INTEGRATING LASER PLASMA ACCELERATED PROTON BEAMS AND THERMOACOUSTIC IMAGING INTO AN IMAGE-GUIDED SMALL ANIMAL THERAPY PLATFORM

by

Michael J. Vieceli

A Thesis

Submitted to the Faculty of Purdue University

In Partial Fulfillment of the Requirements for the degree of

Master of Science

School of Health Sciences

West Lafayette, Indiana

May 2022

THE PURDUE UNIVERSITY GRADUATE SCHOOL

STATEMENT OF COMMITTEE APPROVAL

Dr. Keith Stantz, Chair

School of Health Sciences

Dr. Linda Nie

School of Health Sciences

Dr. Ahmed Hassanein

School of Nuclear Engineering

Approved By:

Dr. Aaron Bowman

Dedicated to my family and friends who have supported me throughout my master's studies at Purdue University

ACKNOWLEDGEMENTS

I would like to first and foremost thank Dr. Keith Stantz for being my MS Thesis advisor and mentor throughout my time at Purdue. I have grown a lot as a researcher under his guidance and have had the opportunity to work on a very exciting research topic that I have become passionate about. I am especially grateful for him always being willing to make extra time to help me with research, classes, and advancing in my career.

I would like to thank Dr. Linda Nie and Dr. Ahmed Hassanein for serving on my MS Thesis Committee and for their attention to reviewing my work in this thesis.

I would like to thank my fellow lab member Abdul Almalki for his support in my research and for helping me with FLUKA.

I would like to thank my friend Jacob Rhoda for helping me install a Linux virtual box, install FLUKA/Flair, and for helping me learn to code in C++.

Last but not least, I would like to thank my family and friends who have supported and encouraged me throughout my MS studies at Purdue and continue to as I prepare for the next step in becoming a medical physicist.

This thesis was prepared by Michael Vieceli under award 31310019M0032 from the School of Health Sciences, Purdue University, Nuclear Regulatory Commission. The statements, findings, conclusions, and recommendations are those of the author(s) and do not necessarily reflect the view of the School of Health Sciences, Purdue University, or the U.S. Nuclear Regulatory Commission.

TABLE OF CONTENTS

LIST OF FIGURES

LIST OF ABBREVIATIONS

CSDA	Continuously slowing down approximation
DVH	Dose volume histogram
FFT	Fast Fourier transform
FOV	Field of view
FT	Fourier transform
FWHM	Full-width half-max
IFT	Inverse Fourier transform
LET	Linear energy transfer
LPA	Laser plasma accelerated/acceleration
MC	Monte Carlo
NIST	National Institute of Standards and Technology
OAR	Organ at risk
PDD	Percent depth dose
PET	Positron emission tomography
PIC	Particle in cell
PTV	Planning target volume
QA	Quality assurance
RBE	Radiobiological/relative biological effectiveness
RPA	Radiation pressure acceleration
SOBP	Spread-out Bragg peak
SSD	Source to surface distance
TNSA	Target normal sheath acceleration

ABSTRACT

Proton beam therapy has shown great promise for cancer treatment due to its high precision in irradiating tumor volumes. However, due to the massive size and expense of the cyclotrons/synchrotrons needed to accelerate the protons, the widespread use of proton therapy is limited. Laser plasma accelerated (LPA) proton beams may be a potential alternative to conventional proton beams: by shooting an ultraintense, ultrashort pulsed laser at a thin target, a plasma sheath electric field may be formed with the capability of accelerating protons to potentially therapeutic energies in very short distances. In addition to accessibility, there is significant uncertainty in proton range in heterogeneous tissues. Thermoacoustic computed tomographic (TACT) imaging has the potential to provide *in vivo* dose imaging and range verification to address these uncertainties. TACT measures thermoacoustic waves generated from the absorbed dose and implements a 3D filtered backprojection to reconstruct volumetric images of the dose. The purpose of this thesis is to determine the feasibility of integrating LPA proton beams with thermoacoustic imaging into a novel image-guided small animal therapy platform as an early step towards clinical translation to address the issues of accessibility and dosimetric spatial uncertainty. A Monte Carlo (MC) method is used to simulate an LPA proton beam with characteristics based on literature, thermoacoustic waves are simulated on a voxel-wise basis of the MC dose, and 3D filtered backprojection is used to reconstruct a volumetric image of the dose. In Specific Aim 1, the dependence of image accuracy on transducer array angular coverage is investigated; in Specific Aim 2, an iterative reconstruction algorithm is implemented to improve image accuracy through increased sampling of projection space when transducer array angular coverage is insufficient; and in Specific Aim 3, the detector sensitivity to dose is determined for several therapeutic endpoints. The work presented in this thesis not only demonstrates the feasibility of integrating LPA and thermoacoustic technologies but necessary design changes to realize a functional small animal platform.

CHAPTER 1. INTRODUCTION

Proton beam therapy has shown great promise for cancer treatment, having several distinct advantages over the x-ray beams conventionally used in radiation therapy. X-rays, being neutrally charged, deposit dose in the body according to their attenuation coefficient, resulting in higher entrance dose and an exponentially decreasing dose with depth, and pass through the entire body. Protons, on the other hand, are electrically charged, and deposits dose along its pathlength according to its stopping power. The protons deposit lower entrance dose, most of their dose at the depth of the Bragg peak, and minimal dose beyond its distal edge. The percent depth dose (PDD) for a proton beam is compared to the PDD of an x-ray beam in Figure 1 (left).

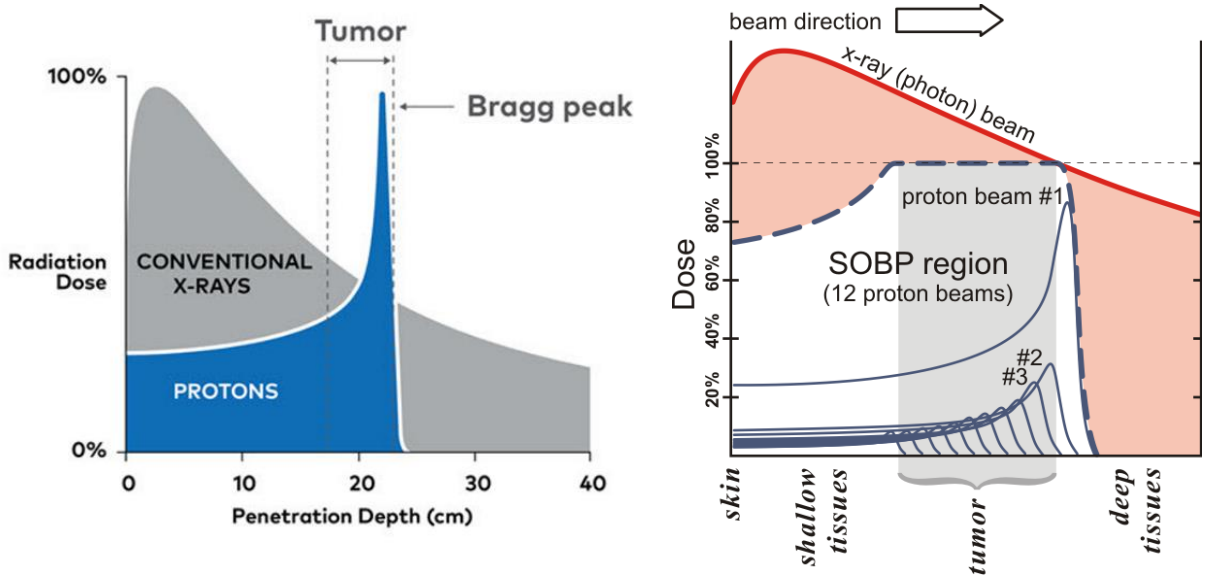

Figure 1: (Left) Percent depth dose (PDD) for protons vs. x-rays (Image source: Varian, *Benefits of Intensity Modulated Proton Therapy*). (Right) Spread-out Bragg peak (SOBP). In this figure, the SOBP and x-ray beam are designed to cover the entire tumor with at 100% or more dose, with the x-ray beam having a higher integral dose with the additional dose shaded in red. Note that the beams in this figure all originate from one direction; multiple x-ray beam angles may be used to decrease the dose to a given area of healthy tissue and organs at risk (OARs), albeit at the expense of irradiating a larger area of healthy tissue and/or OARs (Image source: Wikipedia, *Proton Therapy*).

Proton beams of several different energies can be weighted to achieve a spread-out Bragg peak (SOBP), depositing dose uniformly over the entire tumor volume (target volume) with higher spatial conformality and lower integral dose than x-ray beams (Figure 1, right). Having minimal dose beyond the distal edge of the Bragg peak is particularly advantageous when an organ at risk

is just beyond it (e.g., the brainstem for a brain cancer treatment). The lower integral dose in proton beam therapy also decreases the risk of developing radiation-induced secondary cancers, which is significant for pediatric patients, who have a high rate of developing secondary cancer during their lifetimes.[1] Additionally, protons have a high linear energy transfer (LET) at the Bragg peak and distal edge that may result in higher radiobiological effectiveness (RBEs) for endpoints such as decreasing cell survival or initiating and innate/adaptive immune response.[2]

Although proton beams have these advantages over x-ray beams, the widespread use of proton therapy is limited due to logistical factors. Protons are accelerated to therapeutic energies using cyclotrons/synchrotrons: both use high voltage electric fields to accelerate the protons and magnetic fields to bend their paths circularly until they reach the desired energy and are then sent into patient treatment rooms. Because of the heavy mass of protons, the radius of the cyclotron/synchrotron must be large in order to accelerate the protons to therapeutic energies, making cyclotrons/synchrotrons massive and subsequently expensive (Figure 2).

Figure 2: Cyclotron (left) and synchrotron (right). (Image source (left): OncoLink, *Proton Therapy: Behind the Scenes*. Image source (right): MedGadget, *Hitachi Proton Beam Therapy Coming to Mayo Clinic*.).

Additionally, cyclotrons/synchrotrons are too large to fit into existing x-ray accelerator rooms and thus require a large, dedicated proton facility. The extra cost and required resources make proton beam therapy exclusive to larger institutions; as of 2022, there are only 41 proton centers in the United States (in 2012, there were only 10 proton centers),[3] which limits the number of patients who could benefit from proton therapy.

Laser plasma accelerated (LPA) proton beams may be able to overcome this logistical issue.[4-14] LPA proton beams are created using an ultraintense, ultrashort pulsed laser incident on a thin target, which creates a plasma sheath electric field on the order of tens of MV/μm (TV/m). This electric field gradient has the ability to accelerate protons to therapeutic energies in very short distances. Thus, proton beams can be created with cheaper equipment than cyclotrons/synchrotrons and fit in existing x-ray accelerator rooms. The ability to overcome these logistical issues may allow proton beam therapy to become more available to average radiation oncology clinics and accessible to more patients. However, the inhomogeneity of the LPA electric field results in a broad spectrum of proton energies, limiting the ability of LPA proton beams to achieve the same level of dosimetric spatial conformality achievable with cyclotron/synchrotron-produced monoenergetic beams; LPA beams may also have issues with beam angular divergence, reproducibility, and stability. To achieve widespread use, LPA proton beams need to develop beyond the experimental stage, overcoming issues associated with therapeutic beam quality.

Proton therapy plans can be created with high spatial conformality of dose. However, this high spatial conformality is a double-edged sword: a misalignment of the planned dose and the tumor may result in underdosing part of the tumor and overdosing adjacent healthy tissues or OARs. In practice, the distal edge of the proton dose is rarely closely abutted against OARs in treatment plans due to uncertainties in determining the range.[15] Patient specific quality assurance (QA) can be performed to ensure that the delivered beam is the same as the planned beam and that the patient is properly aligned with the beam. Currently in the clinic, there is no way to verify *in vivo* the dose distribution received; real-time *in vivo* dose imaging would allow for making sure the delivered dose is accurate to the treatment plan by determining the uncertainty in the proton's range and allowing one to adapt the patient's treatment.

Several studies have investigated alternative techniques to image dose by detecting prompt gamma rays[15–18] and annihilation photons from positron emitters[15,18,19] created by proton nuclear interactions. The annihilation photons are readily detected by positron emission tomography (PET), and prompt gamma can be detected by detectors similar in principle to gamma cameras (in practice, adequate detectors have not been able to be implemented into the clinic for prompt gammas), which map the locations of the emissions to infer the absorbed dosimetry. These forms of imaging have limited accuracy and sensitivity. Because the generation of positron emitting

radioisotopes requires higher energy protons, the PET signal will correspond more to dose proximal to the Bragg peak or distal edge, so determining the Bragg peak and distal edge positions to sufficient accuracy is dubious.[16] Additionally, the longer acquisition time from the relatively longer half-lives of positron emitting isotopes for PET is more susceptible to motion and biological washout.[18] Prompt gammas show more promise since they are generated by protons at smaller energies (10-20 MeV) with ranges about 1-4 mm,[16] allowing for more accurate dose localization of the Bragg peak and distal edge. They additionally have a higher gamma ray production rate than for positron emitter production.[18] Since prompt gamma detection does not use coincidence detection like PET, neutron capture gamma rays due to proton produced neutrons add noise to the prompt gamma signal.

Alternatively, thermoacoustic imaging provides a direct method to image proton dose.[20–22] The thermoacoustic effect is based on the creation of acoustic pressure waves resulting from thermoelastic volume expansion of the medium caused by local temperature rise due to the deposited dose. Unlike PET or prompt gamma signals that arise from nuclear interactions, thermoacoustic imaging measures signals directly resultant of the absorbed proton dose from collisional stopping power. These thermoacoustic pressure signals can be measured with an array of piezoelectric transducers or hydrophones, and a 3D filtered backprojection algorithm can be used to reconstruct an image of the dose. A previous study in our lab demonstrated the feasibility of thermoacoustic imaging with clinical quality pencil proton beams and found Bragg peak agreement to MC dose within 2%, a hydrophone pressure sensitivity of 38 mPa to detect a 1 cGy Bragg peak, and that an existing hydrophone detector could be able to measure doses as low as 1.6 cGy.[20] Thus, thermoacoustic imaging can provide an order of magnitude greater sensitivity than PET or prompt gamma imaging and potentially submillimeter accuracy, all on a pulse-by-pulse basis.

The purpose of this thesis is to integrate LPA proton beams and thermoacoustic imaging into a novel imaged-guided small animal proton therapy platform. This work serves as a feasibility study as an early step towards the goal of clinical translation to address the issues of proton therapy accessibility and *in vivo* dose verification; an intermediate translational goal is to make this technology available in laboratory settings for non-clinical particle therapy studies. To determine the feasibility of this technology, a modeled LPA proton beam is coupled with a thermoacoustic

detector to determine its ability to accurately image its dosimetric spatial distribution and magnitude. The LPA proton beam is modeled with characteristics based on literature and is simulated with FLUKA, a Monte Carlo software package, and the dose is thermoacoustically imaged via simulation. The dependence of image accuracy on angular coverage is investigated, an iterative reconstruction algorithm is implemented to acquire missing projections for filtered backprojection when angular coverage is insufficient, and the dose sensitivity of the detector is determined for several therapeutic endpoints.

CHAPTER 2. BACKGROUND

2.1 Laser Plasma Acceleration

Laser plasma acceleration (LPA) of protons is achieved by aiming a short-pulsed (~15 fs – 1 ps), ultraintense (10^{19}-10^{23} W/cm^2) laser[4,5,7,9,11–14] at a thin target to create a plasma sheath electric field to accelerate protons from within the target. The laser first heats electrons to high energies through the ponderomotive force, in which electrons oscillate in the electric field of the laser's electromagnetic wave, and the resultant velocity from oscillation results in the electromagnetic wave's magnetic field exerting a Lorentz force on the electrons. Thus, the laser accelerates "hot" electrons in the direction of laser propagation.

The "hot" electrons create a plasma sheath electric field through one or more of several mechanisms. The most studied and reproducible mechanism is the target normal sheath acceleration (TNSA) mechanism.[4,5,7–9,11,13] In the TNSA scheme, the laser accelerates hot electrons from the front of the target through the target and off the rear of the target. The separation of charges between the negatively charged hot electrons posterior to the target and positively charged ions within the target creates a plasma sheath electric field with electric field strength on the order of tens of MV/μm (TV/m).[5,9,12,13] This quasistatic electric field accelerates protons within the target out the rear of the target up to potentially therapeutic energies in a very short distance. In addition to the protons being accelerated, most of the electrons are held back by the pull of the protons.[8] The electric field terminates once the protons and electrons neutralize the space charge.[5] Heavier ions, such as carbon ions, may be accelerated in addition to protons but are slower due to a lower charge-to-mass ratio than protons. By choosing a target with less protons, a greater number of heavier ions may be accelerated before the space charge terminates.[8]

A key characteristic of the TNSA mechanism is that the protons are always accelerated normal to the target. To demonstrate that the proton beams they were achieving were due to the TNSA mechanism, Wagner et al.[7] aimed their laser at the target at different angles and found the proton beams were emitted normally to the target with energy independent of target angle. This property of the TNSA mechanism results in self-collimation of the proton beam. An illustration of the TNSA mechanism is shown below in Figure 3. Also shown below in Figure 3 is the radiation pressure acceleration (RPA) mechanism[6,8] in which the radiation pressure pushes the surface of

the target inwards and results in a plasma sheath electric field that accelerates protons from the front of the target. In contrast to the TNSA mechanism, in which the proton energy scales proportional to $\sqrt{I\lambda^2}$ where I is the laser intensity and λ is the laser wavelength, the proton energy scales proportional to $I\lambda^2$ for the RPA mechanism which means that higher proton energies may be achieved with RPA.[8]

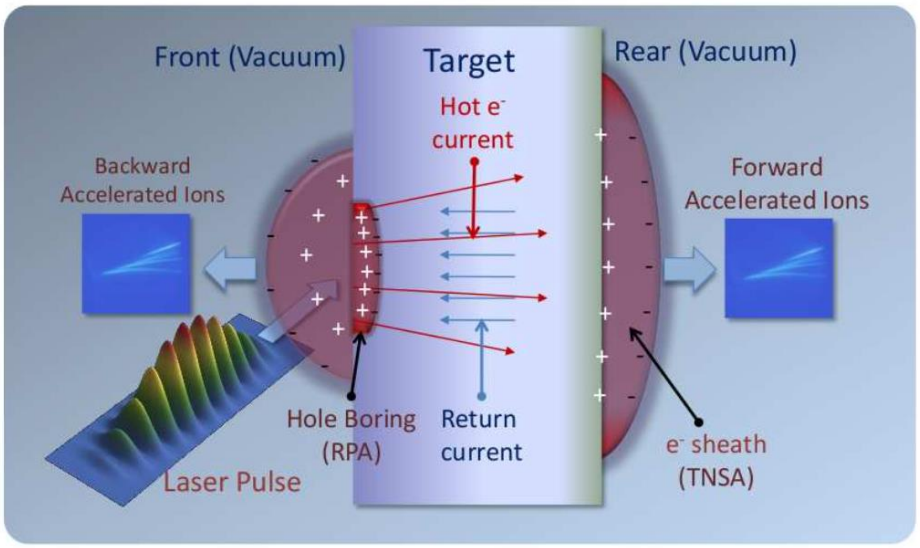

Figure 3: Illustration of the TNSA and RPA mechanisms of laser plasma acceleration (Image source: Macchi et al.[8]).

LPA proton energies of 1.2 MeV,[5] 85 MeV and higher,[7] and 94-101 MeV[9] have been achieved experimentally, and energies of 3.14 MeV and 10.0 MeV,[13] 175 MeV and 350 MeV,[11] and upwards of 1 GeV[14] have been simulated. Most of these energies are below the necessary range of about 200 MeV to 250 MeV needed for proton therapy.[13] Adjusting variables such as laser intensity, acceleration mechanism,[8] pulse width, target type,[5,7,11,14] and target thickness[7,9] may be able to increase the maximum proton energy. However, the plasma sheath electric field is inhomogeneous across the target, resulting in a broadband of energies with a distinct cutoff maximum energy.[8] In contrast, proton therapy uses monoenergetic proton beams with a specific range and modulates the energy in order to precisely irradiate tumors at different depths. Because of this, the wide energy spread of LPA protons beams is perhaps the greatest challenge to be overcome for therapeutic use. In order to overcome the broadband energy issue, Schwoerer et al.[5] placed a small, proton-rich polymethylmethacrylic (PMMA) "dot" on the backside of the target

with a diameter smaller than the laser focus diameter so that the protons in the PMMA dot experienced a more uniform electric field. They were able to achieve a peak energy of 1.2 MeV instead of a pseudo-exponentially decreasing energy spectrum. However, the peak had a full-width half-maximum (FWHM) energy spread of 25%. Meinhold et al.[6] found FWHMs of 12% and 26% for the RPA mechanism, and several other groups have reported wide continuous energy spectrums.[7–11] Thus, while energy peaks have been achieved, the energy spread currently remains too wide for clinical use.

It is also important that the LPA proton beam has enough protons/pulse, with about 10^9 protons/pulse needed.[4] Protons/pulses that have been achieved include 10^7 protons at a 1.2 MeV peak and 10^8 protons/msr,[5] 10^8 protons between 100-350 MeV,[11] 10^{11} protons,[10] and 10^9-10^{12} protons/MeV-sr.[9] Thus, LPA should be able to produce a sufficient number of protons/pulse, although pulse rates are as low as 10 Hz.[4,5] Additionally, despite the self-collimation of the TNSA mechanism, there is still angular divergence due to inhomogeneities in the plasma sheath electric field and target deformation from the pulse.[4,5,11,13] Other concerns about LPA are its stability, with the possibility that a single pulse can break the target,[4] and its reproducibility, with reports that peak energy and energy spread have varied by ±20% from shot to shot.[5]

In summary, while LPA has the potential to produce high enough energy beams with enough protons/pulse, the beam quality does not meet clinical standards due to wide energy spreads, angular divergence, system stability, and reproducibility. Despite the lower beam quality, Schell et al. designed a hypothetical proton therapy system that uses energy and fluence selection for treatment plans using clustering.[23] Instead of pencil beam scanning in which single spots are individually irradiated, a cluster of spots can be irradiated simultaneously by selecting a beam energy window and modulating the lateral beam fluence. By implementing their clustering algorithm into a treatment planning system, they showed on dose volume histograms (DVHs) that planning tumor volumes (PTVs) can be covered excellently and that dose to OARs is comparable to conventional pencil beam treatment plans. Thus, it may not be necessary to try to achieve conventional quality proton beams in order to achieve good treatment plans with LPA.

2.2 Thermoacoustic Imaging

2.2.1 Thermoacoustic Pressure Waves

When protons deposit dose into a medium, the protons' energy is transferred to electrons. Whatever energy the electrons have after ionizing/exciting other atoms/molecules ends up as thermal energy that is absorbed by the medium. The amount of heat conducted into or out of a small volume in the medium is equal to the amount on heat absorbed from external sources (e.g., proton beams) minus the change in stored thermal energy. When heat is absorbed over a long time, most of the absorbed heat is conducted out of the volume, resulting in a relatively constant temperature. When the heat is absorbed in a short pulse (< ~10 μs), which is the case for LPA proton beam pulses, the amount of heat stored in the volume is much greater than the amount of heat that is conducted out of the volume, such that conduction is negligible. The change in temperature in the volume due to absorbed heat from proton dose is then

$$q_{ext} = \rho c \frac{\partial T(\vec{r}, t)}{\partial t} \quad \text{Eq. 1}$$

where q_{ext} is the rate of absorbed heat, ρ is the density of the medium, c is the specific heat of the medium, T is the temperature of the volume, $\vec{r}$ is the position of the volume, and t is time. The resultant temperature increase must do work in the form of volume expansion. The volume expansion is dependent on both the temperature of the volume and the pressure from the surrounding medium resisting the volume expansion, as shown below in Eq. 2

$$\frac{dV}{V} = \vec{\nabla} \cdot \vec{u} = -\kappa_T p(\vec{r}, t) + \beta T(\vec{r}, t) \quad \text{Eq. 2}$$

where V is the volume, dV is the differential volume increase, $\vec{u}$ is the acoustic displacement vector, κ_T is the isothermal compressibility coefficient, p is the pressure the surrounding medium exerts on the volume, and β is the isobaric thermal expansivity coefficient.

Inserting Eq. 2 into Newton's second law, ignoring sheer forces, and plugging in Eq. 1 results in a wave equation, shown below in Eq. 3

$$\left(\frac{1}{v_s^2}\frac{\partial^2}{\partial t^2} - \vec{\nabla}^2\right) p(\vec{r}, t) = \frac{\Gamma}{v_s^2}\frac{\partial q_{ext}(\vec{r}, t)}{\partial t} \quad \text{Eq. 3}$$

where $v_s = \frac{1}{\sqrt{\rho \kappa_T}}$ is the speed of sound in the medium (v_s = 1.5 mm/μs in water) and $\Gamma = \frac{\beta v_s^2}{c}$ is the Gruneisen coefficient, which converts from dose to pressure (Γ = 107 Pa/Gy in water). Using a time-retarded Green's function, the solution to Eq. 3 is found to be

$$p(\vec{r}, t) = \frac{\Gamma v_s^{-2}}{4\pi} \iiint \frac{d^3 r'}{|\vec{r} - \vec{r}'|} \left(\frac{\partial q_{ext}(\vec{r}', t')}{\partial t} \right)_{t' = t - \frac{|\vec{r} - \vec{r}'|}{v_s}} \quad \text{Eq. 4}$$

where $|\vec{r} - \vec{r}'|$ is the distance between the point of dose deposition ($\vec{r}'$) and point of thermoacoustic wave measurement (i.e., a transducer at $\vec{r}$), and $t' = t - \frac{|\vec{r} - \vec{r}'|}{v_s}$ is the retarded or propagation time (i.e., the time it takes the thermoacoustic wave to travel from the point of dose deposition to a transducer). Since heat conduction is negligible, $q_{ext}(\vec{r}', t')$ can be separated into spatial and temporal components such that

$$q_{ext}(\vec{r}', t') = D(\vec{r}')\tau(t') \quad \text{Eq. 5}$$

where $D(\vec{r}')$ is the absorbed dose at position $\vec{r}'$ and $\tau(t')$ is the temporal shape of the proton pulse at time t'. For an LPA proton beam with an ultrashort pulse (~fs-ps), we can assume that $\tau(t') = \delta(t - t')$, that is, all the dose is deposited instantaneously. Then the pressure wave is calculated as

$$p(\vec{r}, t) = \frac{\Gamma}{4\pi} \frac{\partial}{\partial r} \iiint \frac{d^3 r'}{|\vec{r} - \vec{r}'|} D(\vec{r}') \delta(|\vec{r} - \vec{r}'|) \quad \text{Eq. 6}$$

since $\delta(t - t') = v_s \delta(|\vec{r} - \vec{r}'|)$ and $\frac{\partial}{\partial t} = v_s \frac{\partial}{\partial r}$.

2.2.2 3D Filtered Backprojection Algorithm

To reconstruct an image of the dose from measured pressure signals, we first define a velocity potential such that

$$\phi(\vec{r}, t) = -\frac{1}{\rho} \int_0^t p(t')\, dt' \quad \text{Eq. 7}$$

where $\phi(\vec{r}, t)$ is the velocity potential at $\vec{r}$ (i.e., position of transducer), ρ is the density of the medium, and $p(t')$ is the measured pressure signal over time t. Plugging Eq. 4 into Eq. 7 yields

$$\phi(\vec{r},t) = -\frac{\Gamma v_s^{-2}}{4\pi\rho}\iiint \frac{d^3r'}{|\vec{r}-\vec{r}'|} q_{ext}(\vec{r}',t'). \quad \text{Eq. 8}$$

Plugging in Eq. 5 and rewriting the temporal component in spatial terms, as was done in Eq. 6, yields

$$\phi(\vec{r},t) = -\frac{\Gamma v_s^{-2}}{4\pi\rho}\iiint \frac{d^3r'}{|\vec{r}-\vec{r}'|} D(\vec{r}')v_s\delta(|\vec{r}-\vec{r}'|). \quad \text{Eq. 9}$$

Because the volume integral is only non-zero at the radius $|\vec{r}-\vec{r}'| = v_s(t-t')$, it can be rewritten as a surface integral as shown below in Eq. 10

$$\phi(\vec{r},t) \approx -\frac{\Gamma v_s^{-2}}{4\pi\rho} v_s \oiint_{|\vec{r}-\vec{r}'|=v_s(t-t')} \frac{D(\vec{r}')}{v_s(t-t')} dS. \quad \text{Eq. 10}$$

Eq. 10 can be related back to Eq. 7:

$$\phi(\vec{r},t) = -\frac{1}{\rho}\int_0^t p(t')\,dt' \approx -\frac{\Gamma v_s^{-2}}{4\pi\rho} \oiint_{|\vec{r}-\vec{r}'|=v_s(t-t')} \frac{D(\vec{r}')}{(t-t')} dS. \quad \text{Eq. 11}$$

The projection of the dose is then defined as

$$\lambda_{\hat{n}} = \oiint_{|\vec{r}-\vec{r}'|=v_s(t-t')} D(\vec{r}')\,dS = 4\pi\frac{(t-t')}{\Gamma v_s^{-2}}\int_0^t p(t')\,dt' \quad \text{Eq. 12}$$

where $\lambda_{\hat{n}}$ is the projection with normal vector $\hat{n}$. The first part of Eq. 12 defines the projection of the dose as measured at a transducer since the signals from the parts of the dose at the same radius will all arrive at the transducer at the same time. The second part of Eq. 12 is equivalent to the definition of the projection in terms of the measured pressure signals. Thus, the dose, which we want to reconstruct an image of, is related to the pressure signals, which we can measure.

Using several projections from different angles that adequately covers projection space, an image of the dose can be reconstructed as

$$D(\vec{r}') = \frac{1}{4\pi^2}\vec{\nabla}^2 \int_{2\pi} d\Omega_n \lambda_{\hat{n}} \equiv \frac{1}{4\pi^2}\int_{2\pi} d\Omega_n \frac{1}{v_s^2}\frac{\partial^2\lambda_{\hat{n}}}{\partial t^2}|_{|\vec{r}-\vec{r}'|=v_s(t-t')} \quad \text{Eq. 13}$$

where the integral is over all the projections. We can write

$$\frac{\partial^2 \lambda_{\hat{n}}}{\partial t^2} = \frac{4\pi|\vec{r}-\vec{r}'|}{\Gamma v_s^{-1}} \frac{\partial^2}{\partial t^2} \int_0^t p(t')dt' = \frac{4\pi|\vec{r}-\vec{r}'|}{\Gamma v_s^{-1}} \frac{\partial}{\partial t} p(t) \quad \text{Eq. 14}$$

where $\frac{(t-t')}{v_s^{-2}} = \frac{|\vec{r}-\vec{r}'|}{v_s^{-1}}$. Given the Fourier transform property

$$\mathrm{FT}\left[\frac{\partial}{\partial t} p(t)\right] = \omega P(\omega) \quad \text{Eq. 15}$$

and letting ω be part of the more general filter function $H(\omega)$ (described below), Eq. 13 can be written as

$$D(\vec{r}') = \frac{1}{\pi \Gamma v_s} \int_{2\pi} d\Omega_n |\vec{r}-\vec{r}'| \cdot \mathrm{IFT}[P(\omega)H(\omega)] \quad \text{Eq. 16}$$

where IFT[·] denotes the inverse Fourier transform.

The reconstructed dose image in Eq. 16 is dependent on the pressure $p(t')$ in the temporal domain or $P(\omega)$ in the frequency domain. However, $p(t')$ or $P(\omega)$ is not the theoretical pressure signal described in Eq. 6, but rather, it is the pressure signal measured by the transducers convolved with the transducer impulse response. The impulse response of the transducer is the signal a transducer measures when exposed to a very short (impulse) signal containing a full spectrum of frequencies. Ideally, the transducer would measure the impulse signal perfectly, which would correspond to a bandwidth capable of measuring all frequencies with equal sensitivity. However, transducers cannot perfectly measure the impulse signal, corresponding to a frequency spectrum with a central frequency at which the transducer is most sensitive to and a bandwidth with sensitivity falling off on either side of the central frequency. If the impulse response is known, the measured pressure signals can be deconvolved with the impulse response to obtain the actual pressure signals:

$$p(t') = p'(t') \otimes \iota(t') \rightarrow \mathrm{FT} \rightarrow P(\omega) = P'(\omega)I(\omega) \rightarrow P'(\omega) = \frac{P(\omega)}{I(\omega)} \quad \text{Eq. 17}$$

where the impulse response convolved pressure is $p(t')$ and $P(\omega)$ in the temporal and frequency domains, respectively, $p'(t')$ and $P'(\omega)$ is the actual pressure signal, $\iota(t')$ and $I(\omega)$ is the impulse response, and FT denotes a Fourier transform.

While this corrects for the impulse response, additional corrections need to be made to the projections. An unfiltered backprojection results in a $1/r$ falloff in the reconstructed object's (i.e.,

dose's) intensity from the detector's isocenter, which is about a $1/\omega$ falloff in the frequency domain. A ramp function, $|\omega|$, is used to correct for this falloff such that $|\omega|\frac{1}{\omega} = 1$. This is taken care of by the ω in Eq. 15, which we let be part of the filter function $H(\omega)$. The ramp function, in addition to correcting for this falloff, also amplifies higher frequencies which may include noise. To correct for this, an apodizing function is used to "roll off" the amplification of higher frequencies to limit noise amplification. The filter function applied to the measured pressure signals, including impulse response correction, is

$$H(\omega) = |\omega|\frac{A(\omega)}{I(\omega)} \qquad \text{Eq. 18}$$

where $H(\omega)$ is the filter function, $|\omega|$ is the ramp function, $A(\omega)$ is the apodizing function, and $I(\omega)$ is the impulse response. This is the filter function defined in Eq. 16. Note that the apodizing function is not needed in the absence of noise (which is only practical for theoretical simulations).

CHAPTER 3. METHODS

3.1 LPA Proton Beam

3.1.1 Monte Carlo

A Monte Carlo (MC) method was used to simulate the LPA proton beam. Based on probability distributions of a random variable, a MC method randomly selects a value of the random variable to be used as an input to a model of an experiment with stochastic dependencies for a given trial and an outcome is determined. When a very large number of trials have been performed, the aggregate of the outcomes represents the expected results of the experiment, with an increasing number of trials resulting in greater precision. Because radiation interactions with matter are stochastic in nature, a MC method can appropriately model radiation transport.[24] MC methods are considered the "gold standard" for the calculation of radiation dosimetry, having been verified to be the most accurate method available and does not require the use of highly complex, analytical radiation transport equations.[25]

In MC methods of radiation transport, a particle of ionizing radiation (e.g., proton, photon) is "thrown" at a material object and is described by its energy, position, and direction of travel. The MC method randomly chooses how far the particle will travel, based on its interaction probability distribution, before it has an interaction. Where it is determined an interaction will occur, the mode of interaction (e.g., Compton scattering for a photon, inelastic collision for a proton) is randomly determined based on the particle's cross-section (uncharged particles) or stopping power (charged particles). The amount of energy lost (deposited in the medium), new direction of travel, and distance until next interaction are then determined, with interactions occurring until the particle has less energy than a predetermined cutoff energy. This algorithm works well for uncharged particles, which have sparse interactions, but it is computationally unrealistic to model every interaction for charged particles, which have numerous interactions. Instead, only the "significant" interactions (e.g., hard collisions) are individually modeled, and the energy deposited between significant interactions is determined as the aggregate of all the interactions that would occur between. Secondary radiations, such as secondary electrons, Bremsstrahlung, characteristic x-rays, etc., may be generated along the path of a primary particle

and their dose subsequently simulated after the primary particle. After a very large number of particles are "thrown" at the object, the dosimetry from each individual particle adds up to form the dosimetry of the entire beam.[24]

3.1.2 FLUKA

The Monte Carlo software package FLUKA[26] was used to simulate the LPA proton beams. FLUKA was developed by the European Organization for Nuclear Research (CERN) and the Italian Institute for Nuclear Physics (INFN) for the simulation of charged particles and has been extensively used for medical physics applications. The electronic stopping power for charged particles is determined by the Bethe-Bloch equation, which for heavy charged particles is

$$\left(\frac{dE}{dx}\right) = 4\pi r_e^2 m_e c^2 \rho N_A \cdot \frac{Z}{A} \cdot \frac{z_{eff}^2}{\beta^2} \cdot f(\beta) \qquad \text{Eq. 19}$$

where r_e is the classical electron radius, $m_e c^2$ is the rest mass energy of an electron, ρ is the density of the medium, N_A is Avogadro's number, Z is the atomic number, A is the average atomic weight, z_{eff} is the effective charge of the heavy charged particles ($z_{eff} = z$ for protons), $\beta = \frac{v}{c}$ is the ratio of the particle's velocity to the speed of light, and $f(\beta)$ is a complicated function that accounts for several corrections including but not limited to the density and shell corrections. In FLUKA, no approximations of $f(\beta)$ are made in order to maintain accuracy. FLUKA also accounts for energy straggling, secondary particle production, multiple Coulomb scattering for primary and secondary particles, and nuclear interactions. The PRECISIOn default, used in this thesis, includes delta ray production with a 100 keV threshold, low energy neutron transport, heavy particle electron-positron production, bremsstrahlung with a 300 keV threshold, and heavy fragment transport.

The FLUKA depth dose and lateral dose has been extensively compared to measured data and has shown tremendous agreement. Simulations for proton and carbon ions have been compared to measurements at the Heidelberg Ion Therapy Center (HIT) and had average dose-weighted dose-differences of 1% and 1.5%, respectively.[26] Notably, this agreement for carbon ions also includes fragmentation dose beyond the distal edge of the Bragg peak. The success of FLUKA has resulted in it being used clinically for independent dose verification and inputs into treatment planning systems.

3.1.3 LPA Beam Model

The LPA proton beam was modeled with characteristics based on literature. The goal in this thesis is not to necessarily replicate an LPA proton beam presented in an individual journal article, nor to implement a particle in cell (PIC) simulation to simulate the generation of an LPA proton beam, but rather to include the key characteristics that can affect the production and detection of thermoacoustic waves such as a wide energy spread,[4–11] angular divergence,[4,5,11,13] and number of protons per pulse.[5,7,9–11] Notably, Eq. 6 shows that the thermoacoustic signal frequency depends on the gradient of the dose, with a wide energy spread contributing to a less steep gradient that results in lower frequency signals. Since the detection of signals with different frequencies depends on the bandwidth of the transducers, the lower frequency LPA thermoacoustic signals will be detected differently than higher frequency monoenergetic proton beams.

The average proton energy was chosen to be 50 MeV, which has a monoenergetic continuously slowing down approximation (CSDA) range of 2.227 cm in water (NIST)[27] and is suitable for treating small animal tumors. The energy spread was set to a Gaussian distribution with a 30% FWHM[4,5] (15 MeV), the angular divergence was set to 2°,[11] and the number of protons per pulse was set to 10^7 protons/pulse[5,11] as a lower bound to how many can be achieved (note that some of these quantities are estimated from figures). The proton beam was aimed perpendicularly at a water phantom with a 100 mm source to surface distance (SSD), in which the pre-phantom medium was selected to be vacuum. Assuming the LPA proton beam originates from a point source (which is reasonable since the laser focal point is on the order of a few micrometers[5,7,11,13] and the voxel size is 0.1 mm), the beam diameter at the entrance of the water phantom was 0.3491 cm. The dosimetry was measured using a USRBIN (the FLUKA tool for scoring dose) with transverse dimensions 1 cm x 1 cm and longitudinal dimension of 4 cm. 100 bins were used in the transverse dimension and 400 in the longitudinal dimension (100 x 100 x 400) such that the voxel side length was isotropically 0.1 mm. Longitudinal and transverse cross-section images of the dose are shown below in Figure 4. Note that the dose is longitudinally oriented traveling in the "negative z-direction" since the transducer arrays (discussed later) are situated in the "negative z-direction" facing the "positive z-direction" (Figure 4 left). The transverse cross-section (Figure 4 right) is at the depth of the Bragg peak.

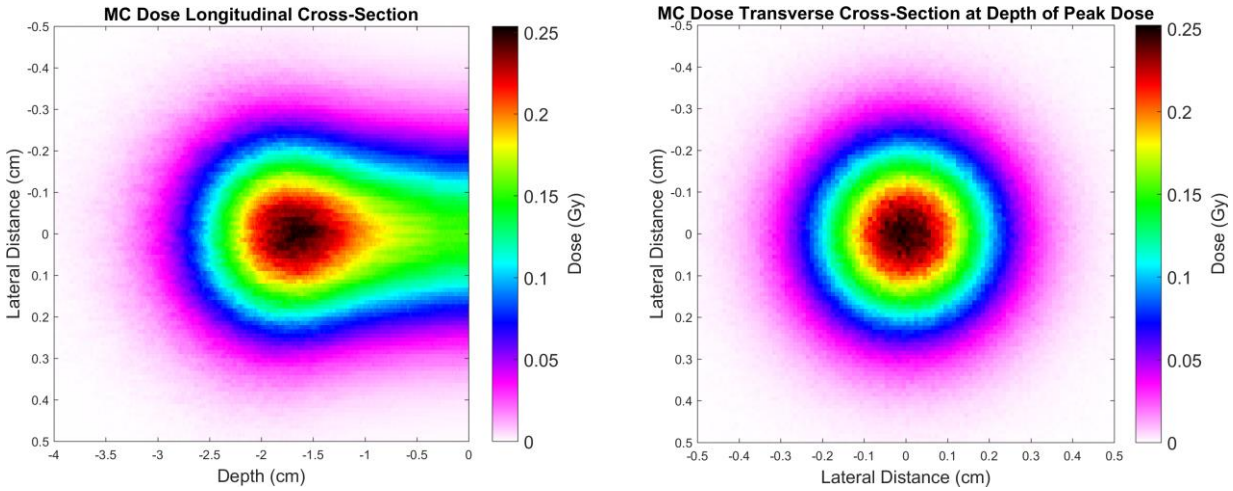

Figure 4: LPA proton beam dose simulated with FLUKA. The transverse cross-section (right) is at the depth of the Bragg peak.

3.2 Thermoacoustic Pressure Wave Simulation

Thermoacoustic pressure waves were simulated on a voxel-wise basis of the FLUKA dose. Subsampling within the voxel was performed to get better sampling from each voxel to achieve clearer signals, with three subsamples per voxel direction (27 subsamples total), and the signal from each voxel was normalized to the number of subsamples. For each transducer in the transducer array, the thermoacoustic signal contributions from each voxel as measured at the transducer location were simulated based on Eq. 6 with a 20 MHz sampling frequency (0.05 μs/sample) and a total of 2048 samples. (Note, in practice, the integral in Eq. 6 was performed first while temporally indexing the signal, as a real system would measure, and the derivative applied afterwards, with the derivative being performed over the temporally measured signals considering that $\frac{\partial}{\partial r} = \frac{1}{v_s}\frac{\partial}{\partial t}$). The signal was convolved with the transducer impulse response (which is experimentally known) using a fast Fourier transform (FFT). The signals were simulated for each transducer in the transducer array and was repeated for 30 rotations of the transducer array over 360° (12° increments) to improve sampling.

Examples of theoretical thermoacoustic pressure waves are shown below in Figure 5, and the same signals convolved with the impulse response are shown below in Figure 6.

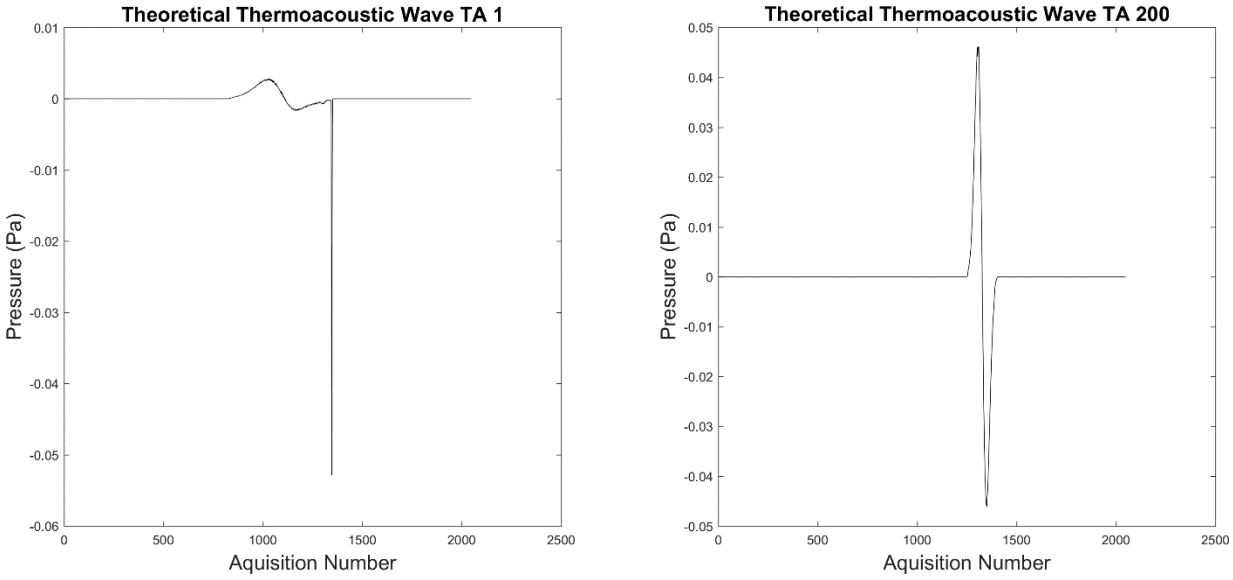

Figure 5: Theoretical pressure wave examples. Left: Signal measured by a transducer that measures a projection parallel to proton beam travel direction. Compression and rarefaction from the dose are shown in the signal followed by a sharp rarefaction spike due to the water edge of the phantom. Right: Signal measured by a transducer that measures a projection lateral to proton beam travel direction. Compression and rarefaction are seen but no water edge rarefaction spike since the projection is parallel to the water edge. Also note that the compression and rarefaction are steeper and have a greater amplitude due to the lateral penumbra being steeper than the distal edge of the Bragg peak (left).

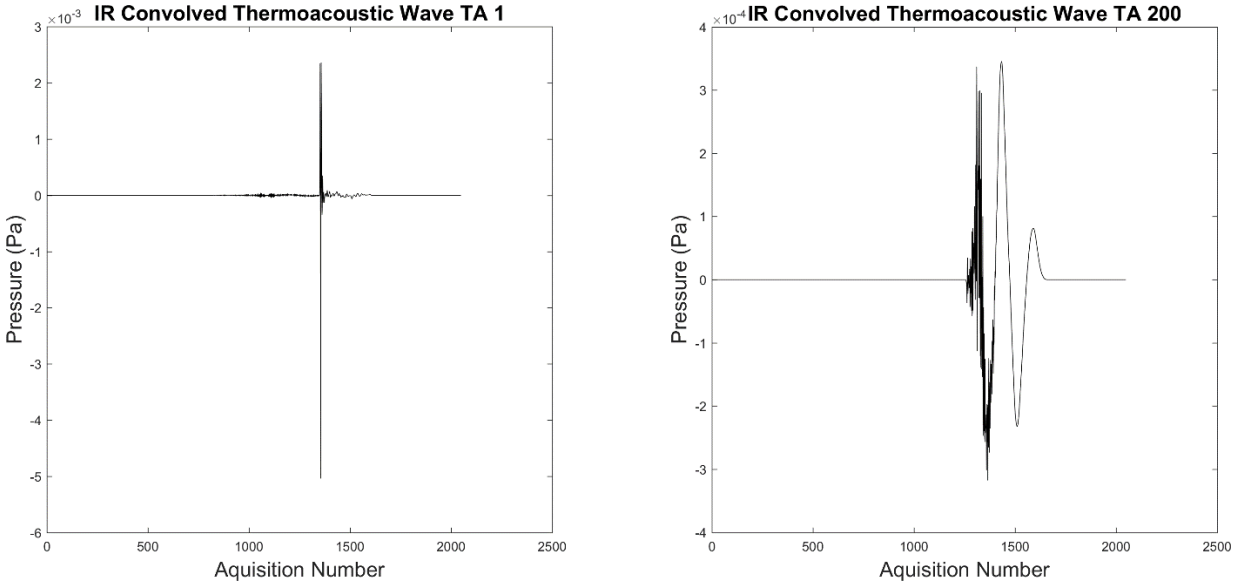

Figure 6: Impulse response (IR) convolved thermoacoustic pressure wave examples. These example signals correspond to the theoretical signals shown above in Figure 5. Due to the bandwidth of the transducers, as measured in the impulse response, lower frequency signals are not detected as well as higher frequencies (~ 5 MHz).

3.3 Image Reconstruction

The simulated thermoacoustic signals were deconvolved with the transducer impulse response, and the ramp and apodizing function were applied to the signals as described in Eq. 18 (note that the apodizing function was only used when noise was added to the signals). These signals were then backprojected as described in Eq. 16 to reconstruct an image of the dose. The image was reconstructed with an additional 1 cm behind the water edge (longitudinal dimension ranging from -4 cm to 1 cm) in order to see the effects of the water edge on image reconstruction. The voxel side length of the reconstructed image was maintained at 0.1 mm. An example of a reconstructed image using a transducer array with 4π angular coverage (most complete sampling possible) is shown below in Figure 7.

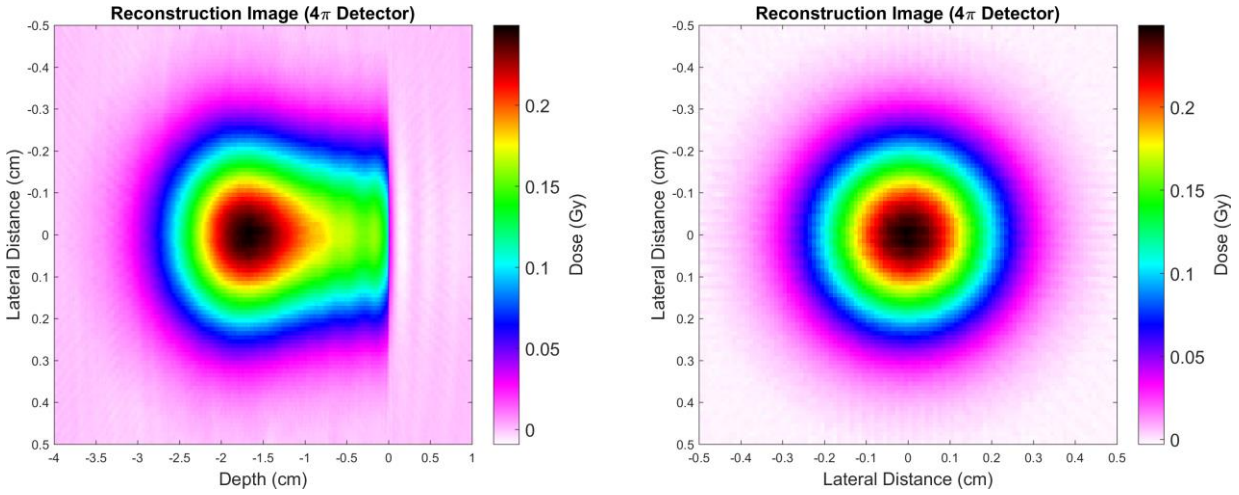

Figure 7: Reconstruction image of the MC dose. Note that image reconstruction with a 4π detector (NEXUS496, discussed later) represents the most complete sampling and upper limit on image accuracy based on filtered backprojection alone.

In practice, the magnitude of the reconstructed dose image was determined using a calibration. This is because the thermoacoustic signal projections are acquired over spherical surfaces instead of planes, and because this filtered backprojection algorithm is based on a 3D Radon transform, the reconstructed dose image is an approximation of the physical dose.[20] A scatter plot of the central axis of the reconstructed dose was compared to the central axis of the MC dose and a linear model was fit to the data to yield a calibration factor. The calibration of a 4π detector (used to reconstruct the image above in Figure 7) is shown below in Figure 8, where, with

the pressure in units of Pa was plotted as a function of reconstructed intensity units, from which the calibration constant was determined to be 2.2812×10^{-5} Gy/reconstruction intensity unit.

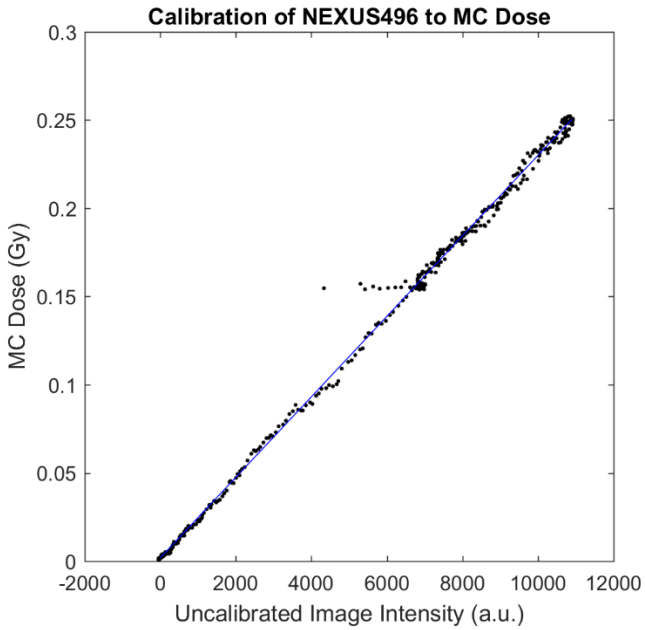

Figure 8: Calibration curve for a 4π detector (NEXUS496, discussed later) to the MC dose. The correlation coefficient $r = 0.9984$ suggests very high correlation between the uncalibrated reconstruction dose and the MC dose, justifying the use of a simple calibration constant. Note that the deviation of the data points near an MC dose of about 0.15 Gy corresponds to the reconstruction image not perfectly matching the water edge and entrance dose just left of 0 cm (see Figure 9, left). Also note that this deviation has minimal effect on the calibration constant. Data points with a depth greater than 0 cm (i.e., the 1 cm extension for the reconstruction image) was not included in the scatter plot.

Figure 9 shows a comparison of the calibrated central axis dose of the 4π detector to the MC dose. Because of the close agreement, the 4π detector was taken to be a control detector, and the calibration constant was assumed to correctly convert from the image intensity inherent to the image reconstruction process described in Eq. 16 to the true dose, and so the calibration constant was applied to all the detectors.

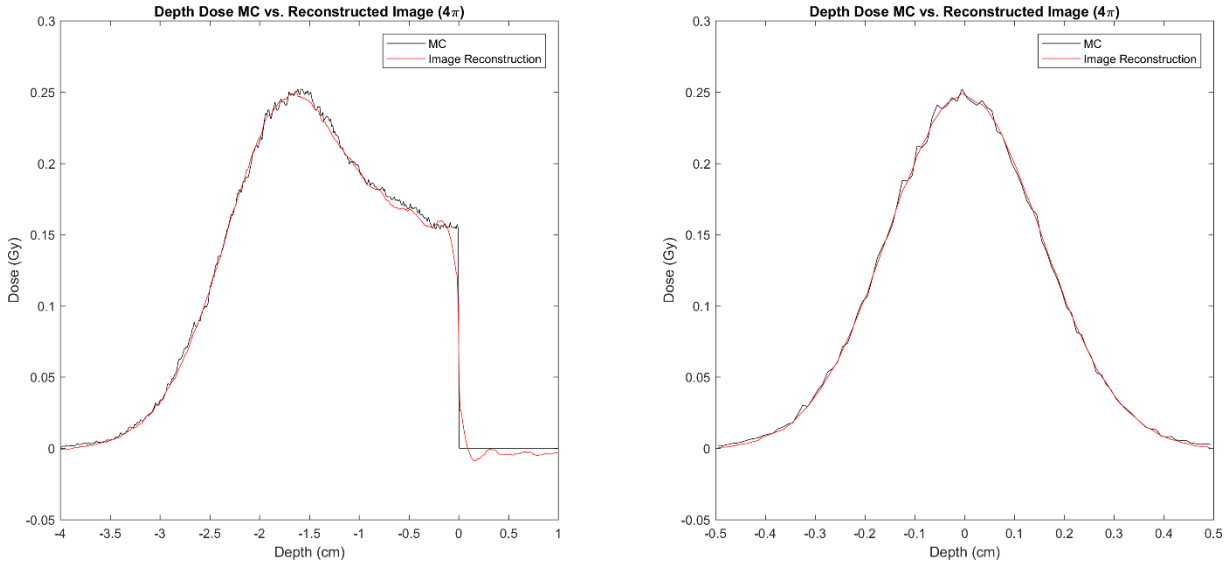

Figure 9: Comparison of reconstructed dose to MC dose. The strong agreement in spatial distribution and magnitude both for the depth dose (left) and lateral profile (right) is the basis for using a 4π detector as a control.

CHAPTER 4. DESCRIPTION OF SPECIFIC AIMS

4.1 Specific Aim 1

The maximum possible angular coverage of a detector is 4π, which has the best projection sampling and will result in the most accurate image reconstruction possible using a filtered backprojection algorithm (Figure 7, Figure 9). However, 4π detectors for external beam therapy dose verification is not physically possible; real detectors may have significantly less angular coverage. Specific Aim 1 of this thesis is to evaluate the dependence of image accuracy on transducer array angular coverage. The transducers of a 4π detector are incrementally turned off to investigate how image accuracy changes with transducer angular coverage. The water level in a 2π detector and a sub-2π detector based on an in-house detector geometry is adjusted in order to get better sampling. The resultant images are compared to the MC PDD.

4.2 Specific Aim 2

As will be made evident in Specific Aim 1, insufficient angular coverage results in reconstruction images that are inadequate for accurate localization of the dose distribution. Iterative reconstruction can be used to improve image accuracy by taking an initial reconstruction image from a sub-4π detector and iteratively simulating signals and reconstructing images to fill in the missing projections. Iterative reconstruction is applied to a sub-2π detector and 2π detector using a 4π detector to simulate the missing projections, and the resultant images are compared to the MC dose.

4.3 Specific Aim 3

The results from Specific Aims 1 and 2 represent theoretical signals. These signals are measured by transducers with a *perfect* response function (infinite bandwidth), in the absence of noise. Detection sensitivity is compromised by an imperfect match between the transducer bandwidth and the bandwidth of the thermoacoustic signal frequencies. Real thermoacoustic measurements also include noise, such as acoustic or electrical noise. The amount of noise present influences the image quality, and too much noise may mask a signal. Conversely, a signal must have a minimum intensity to be detectable beyond baseline noise. Different levels of noise are

added to the thermoacoustic signals and image reconstruction is performed with the implementation of an apodizing function to filter noise. The systematic and statistical errors based on the residuals between the MC dose and reconstruction image are evaluated as a function of noise and are used to determine the sensitivity for several therapeutic endpoints.

CHAPTER 5. SPECIFIC AIM 1

5.1 Introduction

In projection imaging, volumetric spatial information of an object is projected onto a single plane. For example, in radiography, a single projection image is taken and all the anatomy within the field of view (FOV) appear in the image without information about depth; a backprojection of this projection would not provide enough information for a 3D image of the patient. Likewise, a single thermoacoustic projection signal cannot be used to reconstruct a 3D dose image. Rather, projections are measured at several different angles around the object so that enough information is acquired to reconstruct a 3D image. The maximum possible angular coverage is 4π (spherical coverage), in which projections are acquired at all possible projection angles. A 4π detector should theoretically be able to produce a perfect 3D image of an object. However, for applications such as external (proton) beam therapy, the dosimetry being measured in a phantom or patient must be encompassed by the detector, such that a 4π detector would not be physically feasible. Practical detectors would have much less than 4π angular coverage, such as 2π coverage or less.

An in-house detector with 128 transducers, named NEXUS128 (Figure 10), has less than 2π angular coverage, originally built for the purpose of molecular imaging. Another in-house prototype detector has 2π angular coverage. To evaluate the dependence of image reconstruction accuracy on transducer array angular coverage, detector models were evaluated based on these angular coverages (Figure 11). The NEXUS128 model replicates the in-house detector geometry (Figure 10), with each transducer at an equal distance from isocenter (101 mm) and with angular positions such that each projection has equal weighting for the filtered backprojection. The 2π detector, named KMS128 (note that the number in the name of all detectors in this thesis represents the number of transducers in the array), was not modeled after the prototype but rather was designed to have 128 transducers covering 2π with similar geometry to NEXUS128. The KMS256 transducer array was designed to sample 4π of projection space, where the bottom half of the TA follows the KMS128 model and the top half follows a flipped version of the KMS128 model (i.e., two 2π halves of a 4π detector). KMS256 was used as a control as it is expected that the image should be virtually the same as the MC dose.

Figure 10: In-house detector (NEXUS128) with sub-2π angular coverage. The small circles are individual transducers.

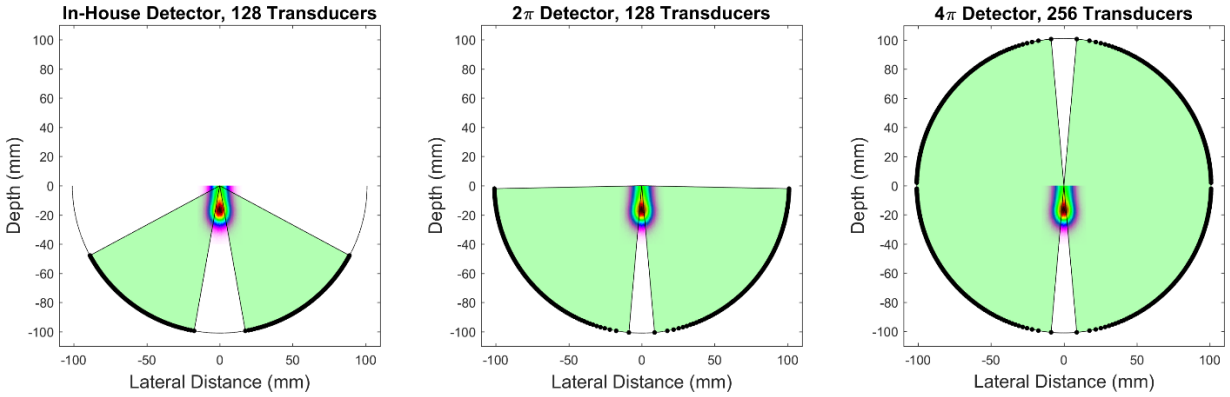

Figure 11: Detector models (for Specific Aim 1). Left: NEXUS128. Middle: KMS128. Right: KMS256. The shaded green areas represent the angular coverage relative to isocenter, and the black dots on the perimeter represent the azimuthal angle of each transducer (note that each half of these illustrations shows the complete number of transducers). Note that this is an illustration and not a full 3D representation of the transducer arrays. The dose shown is the MC dose, representative of the thermoacoustic signal source.

Using the framework described in Section 3 (Methods) of this thesis, the MC dose was imaged by each of the detectors in Figure 11, and the PDD for each reconstruction image is compared to the MC dose PDD displayed in Figure 12.

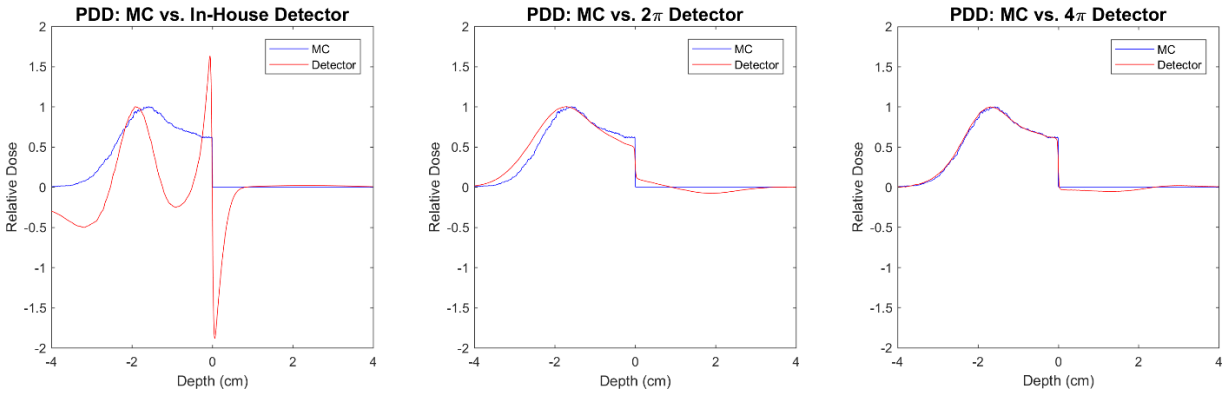

Figure 12: Reconstruction image PDD vs. MC PDD for NEXUS128 (left), KMS128 (middle), and KMS256 (right). KMS256 reconstructs a near perfect image, KMS128 reconstructs a decent image but with deviation at the distal edge and entrance dose, and NEXUS128 reconstructs an inadequate image with a "spike" artifact near 0 cm depth.

As expected, KMS256 reconstructs a near perfect image of the MC dose. KMS128 reconstructs a decent image, although the distal edge and entrance doses deviate from the MC dose. Notably, this deviation at the distal edge can be a significant factor in radiation therapy, since the LET increases affecting DNA damage, cellular death, and immunogenic responses. The reconstructed images using the NEXUS128 design is inadequate, with minimal agreement with the MC dose and a "spike" artifact near 0 cm depth (water level). Thus, while KMS256 demonstrates the feasibility of the imaging technique, KMS128 and NEXUS128 show that lower angular coverages can significantly reduce image accuracy. It is therefore desirable to investigate the dependence of image accuracy on transducer array angular coverage.

It is worth noting that "good enough" accuracy is subjective and depends on the end purpose of the proton beam (e.g., cancer treatment vs. initiating an immune response). For results that are more generalizable, the image accuracy in this thesis is interpreted qualitatively. Aspects that are considered include overall matching of the image reconstruction with the MC dose, which parts of the image reconstruction have good agreement/disagreement (e.g., Bragg peak, distal edge, entrance dose), and the magnitude of the image reconstruction dose.

5.2 Methods

5.2.1 Transducer Array Angular Coverage

In order to get an idea of the angular coverages that will produce good images, transducers in the KMS256 detector were incrementally turned off to reduce the angular coverage. All the transducers below a certain threshold angle θ, defined below in Figure 13, were turned off while the rest were used to acquire projections. Starting with all transducers turned on, the angle between the threshold angle and 90° (at which point the detector becomes 2π) was cut in half. Threshold angles of 0°, 45°, 67.5°, 78.75°, and 84.25° were evaluated. The reconstruction image PDD was then compared to the MC PDD.

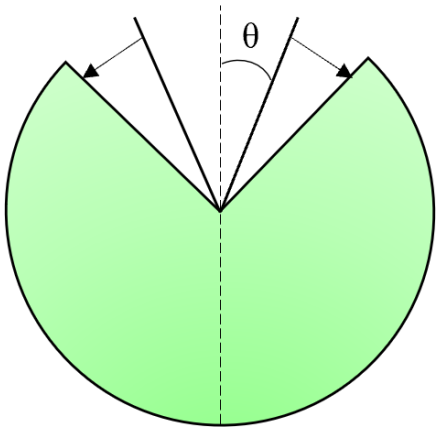

Figure 13: Turning transducers in the KMS256 array off. Detector angular coverages for the threshold angle θ of 0°, 45°, 67.5°, 78.75°, and 84.25° were evaluated.

5.2.2 Water Level Shift

While the angular coverage for the KMS256 detector can be reduced by turning transducers off, the angular coverages of KMS128 and NEXUS128 are limited by design. However, the dose can be shifted further into the detector by lowering the water level, effectively obtaining greater angular coverage for better projection sampling. It is important to note, however, that the best sampling occurs at the detector's isocenter (the isocenter lies at a depth of 0 cm in our detector geometries for all detectors), so moving the dose off isocenter may affect the image accuracy. The benefits of acquiring more effective angular coverage, nevertheless, may outweigh the disadvantages of imaging off isocenter. The water level was lowered from 0 mm by 10 mm, 20

mm, 30 mm, and 40 mm, as illustrated below in Figure 14. This was done for both KMS128 and NEXUS128, and the reconstruction image PDDs were compared to the MC PDD.

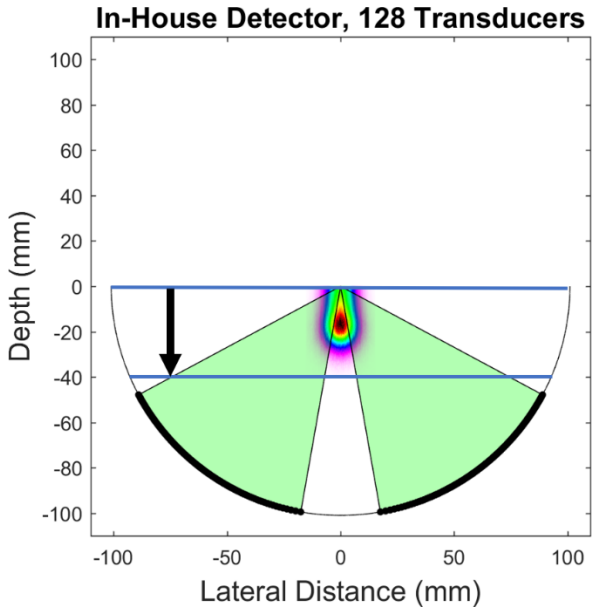

Figure 14: Water level shift. The water level is represented by the blue line and was shifted from a depth of 0 mm to 10 mm, 20 mm, 30 mm, and 40 mm.

5.3 Results

5.3.1 Transducer Array Angular Coverage

The reconstruction image PDDs, using KMS256, are compared to the MC PDD for threshold angles of 0°, 45°, 67.5°, 78.75°, and 84.25°.

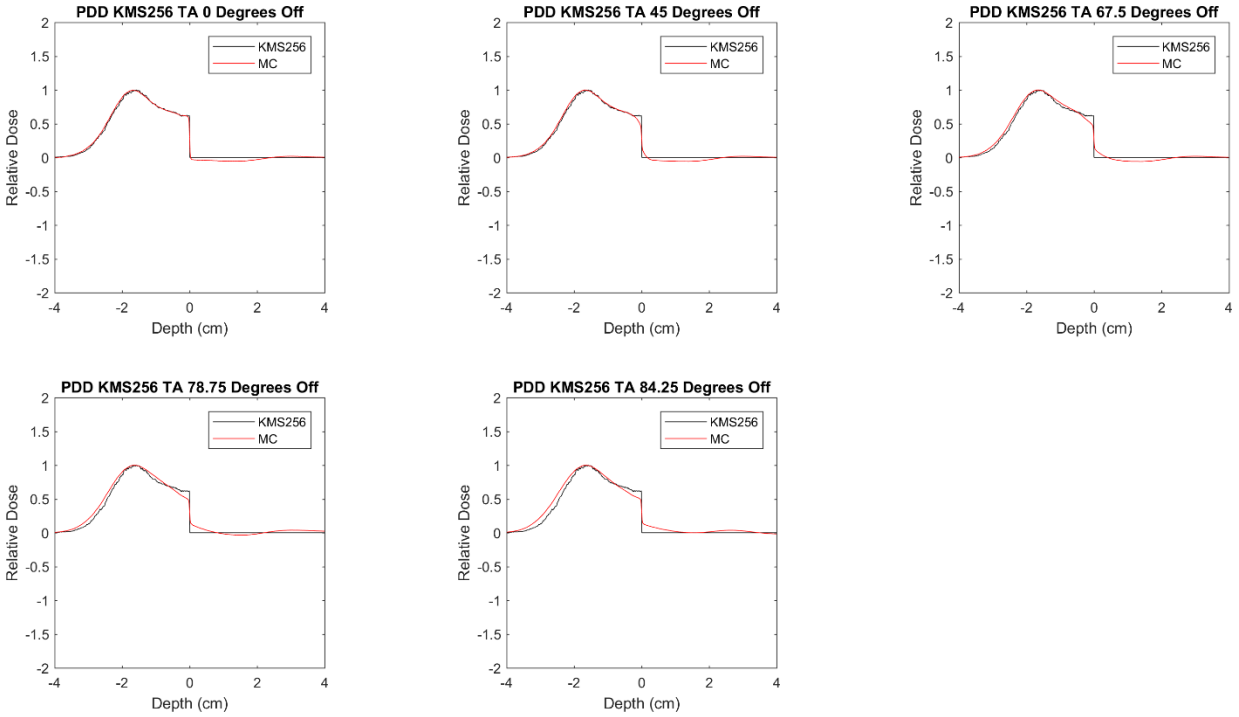

Figure 15: Comparison of the KMS256 PDD and MC PDD for turning off transducers at threshold angles of 0°, 45°, 67.5°, 78.75°, and 84.25°.

5.3.2 Water Level Shift

The reconstruction image PDDs for water level shifts of 0 mm, 10 mm, 20 mm, 30 mm, and 40 mm for KMS128 and NEXUS128 are respectively compared to the MC PDD in Figure 16 and Figure 17.

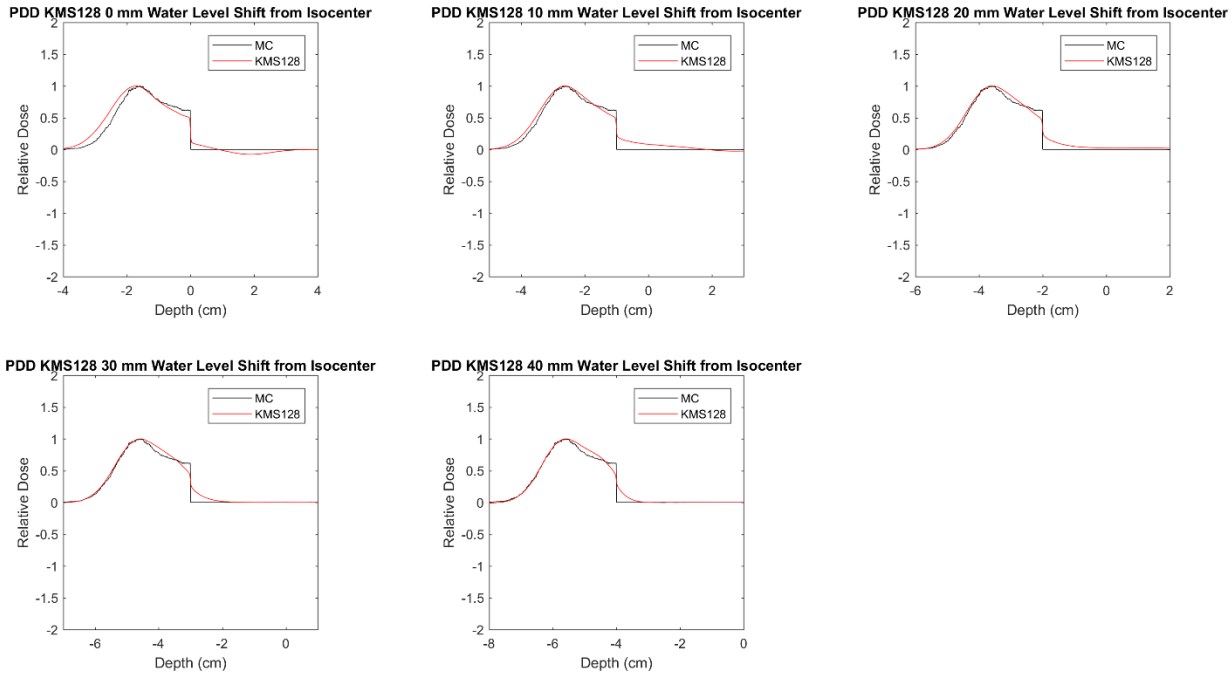

Figure 16: Comparison of the KMS128 PDD and MC PDD for shifting the water level into the detector by 0 mm, 10 mm, 20 mm, 30 mm, and 40 mm.

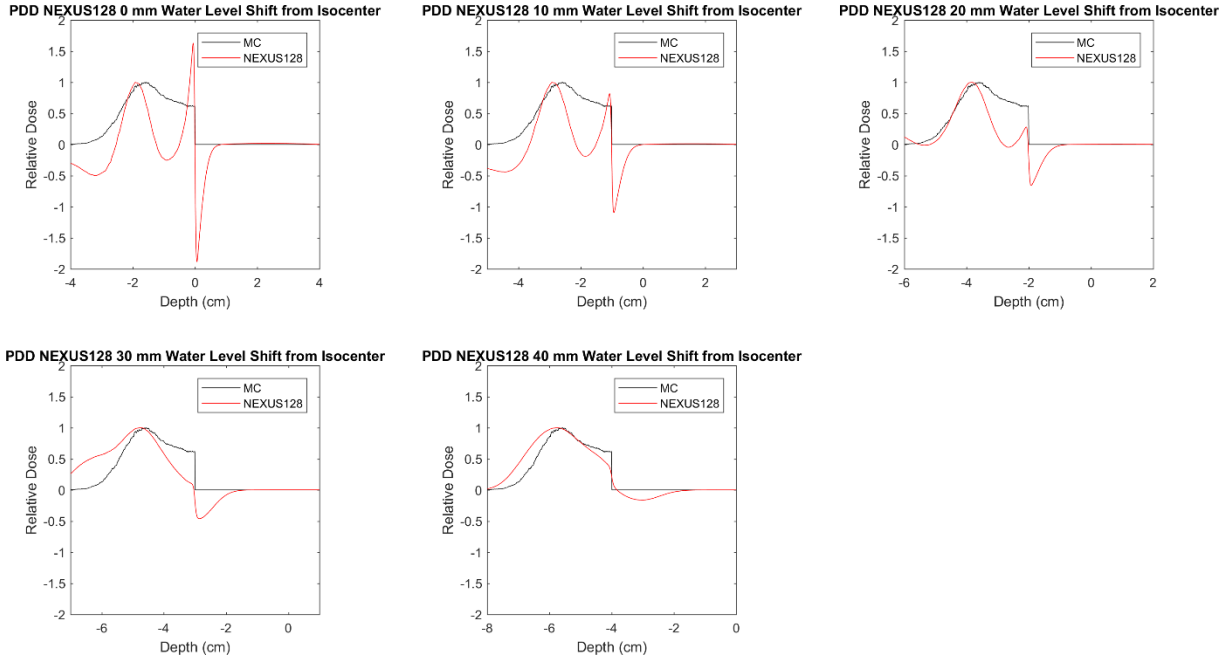

Figure 17: Comparison of the NEXUS128 PDD and MC PDD for shifting the water level into the detector by 0 mm, 10 mm, 20 mm, 30 mm, and 40 mm.

5.4 Discussion

5.4.1 Transducer Array Angular Coverage

Turning transducers off in the KMS256 transducer array was performed as a first step in evaluating angular coverage to provide an idea of what angular coverages can produce accurate images. Shown in Figure 15, the initial image with no transducers turned off is the same as the image in Figure 12 (right) and the last image with 84.25° approaches the image from KMS128 in Figure 12 (middle), which would be 90° off. It is apparent that while the agreement between the reconstruction image and MC dose remains close for most of the images, the agreement decreases to an extent for each decrease in transducer angular coverage. This means that choosing an angular coverage is really a question of what is "good enough." Notably, the Bragg peaks match in all the images. The entrance dose decreases in accuracy for decreasing angular coverage, which may be of little consequence, but the distal edge decreases in accuracy for decreasing angular coverage and may likely be unacceptable in many applications. The results show then that "good enough" angular coverage likely lies between 4π and 2π coverage. This is significant because our in-house detectors have 2π and sub-2π angular coverage. This result is the motivating reason to shift the water level further down in the NEXUS128 and KMS128 detectors in order to effectively increase the angular coverage, although at the expense of moving off isocenter.

5.4.2 Water Level Shift

Shifting the water level downwards for KMS128, shown in Figure 16, improved the image accuracy at the distal edge and maintained accuracy at the Bragg peak, while the accuracy at the entrance dose decreased. The simultaneous improvement in parts of the image and decrease in accuracy in other parts can be attributed to both having better angular coverage and being off-isocenter. Both of these effects should be acting on the entire image, although the weighting of the effects could be different in different parts of the image. It is possible the distal edge further in the detector provides greater angular sampling compared to the entrance dose. This off-isocenter sampling artifact impacts the relative dose between the Bragg peak (and distal edge) and entrance dose. This would be consistent with the on-isocenter images in Figure 15 having the water edge dose decrease in accuracy prior to the distal edge undergoing a decrease in accuracy. Since the Bragg peak and distal edge are typically of greater importance than the entrance dose, an image

with a water level shift may be more desirable. It is also important to note that with the on-isocenter image having decent accuracy, improvement in accuracy by water level shift is limited.

Unlike the KMS128, the entire image when using the NEXUS128 (Figure 17) improved due to the increase in angular sampling, albeit the image accuracy remains unacceptable. While the image accuracy may be insufficient, it is significant that the shape of the image dose went from minimal resemblance of the MC dose to having much better resemblance. It is particularly important to note that the "spike" artifact at the water edge was eliminated with large enough water level shifts (30 mm and 40 mm), which will be of great significance in Specific Aim 2.

5.5 Conclusion

The simulations performed in Specific Aim 1 characterize the dependence of image accuracy on transducer array angular coverage. Transducers in the KMS256 detector were turned off at increasing larger angles and demonstrated how image accuracy decreases from near perfect images at 4π angular coverage to loss of image accuracy to potentially inadequate accuracy as angular coverage approaches 2π. The water level was shifted in towards the detector for KMS128 and NEXUS128, and image accuracy was improved for both, although blurring imperfections due to being off-isocenter were present. Notably, the "spike" artifact from the NEXUS128 image was eliminated for large enough water level shifts. These results, however, show the inadequacy of detectors with significantly less angular coverage than 4π using this framework alone.

CHAPTER 6. SPECIFIC AIM 2

6.1 Introduction

In Specific Aim 1, the sub-4π detectors have insufficient angular coverage to reconstruct adequate images of the proton dosimetry. Lowering the water level into the detector can improve image accuracy but is not enough to reconstruct an image with sufficient quality of dose. Even if shifting the water level far enough into the detector for 4π angular coverage was possible, the image accuracy is limited by blurring due to being off-isocenter. The challenge is to obtain more angular projections.

Iterative reconstruction can be used to fill in the missing projections. Iterative reconstruction is a technique that takes the image reconstructed (the dose) using the physical signals measured by a sub-4π detector and using this information to simulate the missing thermoacoustic signals to form a new image *as if* the dose was imaged by a 4π detector. While the sub-2π NEXUS128 cannot reconstruct a near perfect image, a detector having the same geometry with additional transducers to produce 4π angular coverage would be able to significantly improve image quality and dose. In Specific Aim 2, an iterative reconstruction algorithm is applied to the images from a 2π detector and sub-2π detector in order to achieve convergence to the MC dose.

6.2 Methods

6.2.1 Updated Detectors

In Specific Aim 1, the detectors NEXUS128, KMS128, and KMS256 were evaluated (Figure 11), each having a different angular coverage of sub-2π, 2π, and 4π, respectively. NEXUS128 is modeled to have the geometry of the in-house detector while KMS128 and KMS256 were designed specifically for their angular coverages with equal projection weights. However, the positions of the transducers in KMS128 and KMS256 do not correspond to the positions of the transducers in NEXUS128. In iterative reconstruction, it is essential that the transducer locations in the 4π detector correspond to the transducers in the sub-4π detectors since signals are compared on a transducer-by-transducer basis. Thus, the NEXUS128 is modeled to have the geometry of our in-house detector; the NEXUS248 is modeled to have 2π angular coverage; and the NEXUS496

has 4π angular coverage (note that like KMS256, NEXUS496 is NEXUS248 once on the bottom and once flipped on the top). The geometries of these three detectors are shown below in Figure 18. The reason these detectors were not used in Specific Aim 1 is just due to progression of the project. Note that while the number of transducers and transducer positions are different for NEXUS248 and NEXUS496 than KMS128 and KMS256, their angular coverages are near equivalent; the take-away from Specific Aim 1 should also apply to NEXUS248 and NEXUS496.

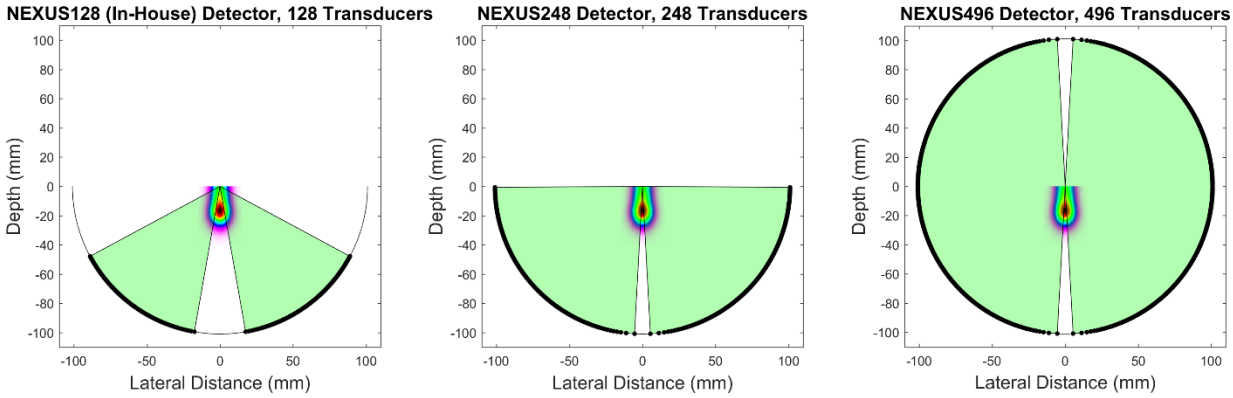

Figure 18: Detector models (for Specific Aim 2). Left: NEXUS128. Middle: NEXUS248. Right: NEXUS496. The shaded green areas represent the angular coverage relative to isocenter, and the black dots on the perimeter represent the azimuthal angle of each transducer (note that each half of these illustrations shows the complete number of transducers). Note that this is an illustration and not a full 3D representation of the transducer arrays. The dose shown is the MC dose, representative of the thermoacoustic signal source. The angular coverages for NEXUS248 and NEXUS496 are near equivalent to those of KMS128 and KMS256, respectively.

6.2.2 Iterative Reconstruction Algorithm

A schematic of the iterative reconstruction algorithm is shown below in Figure 19.

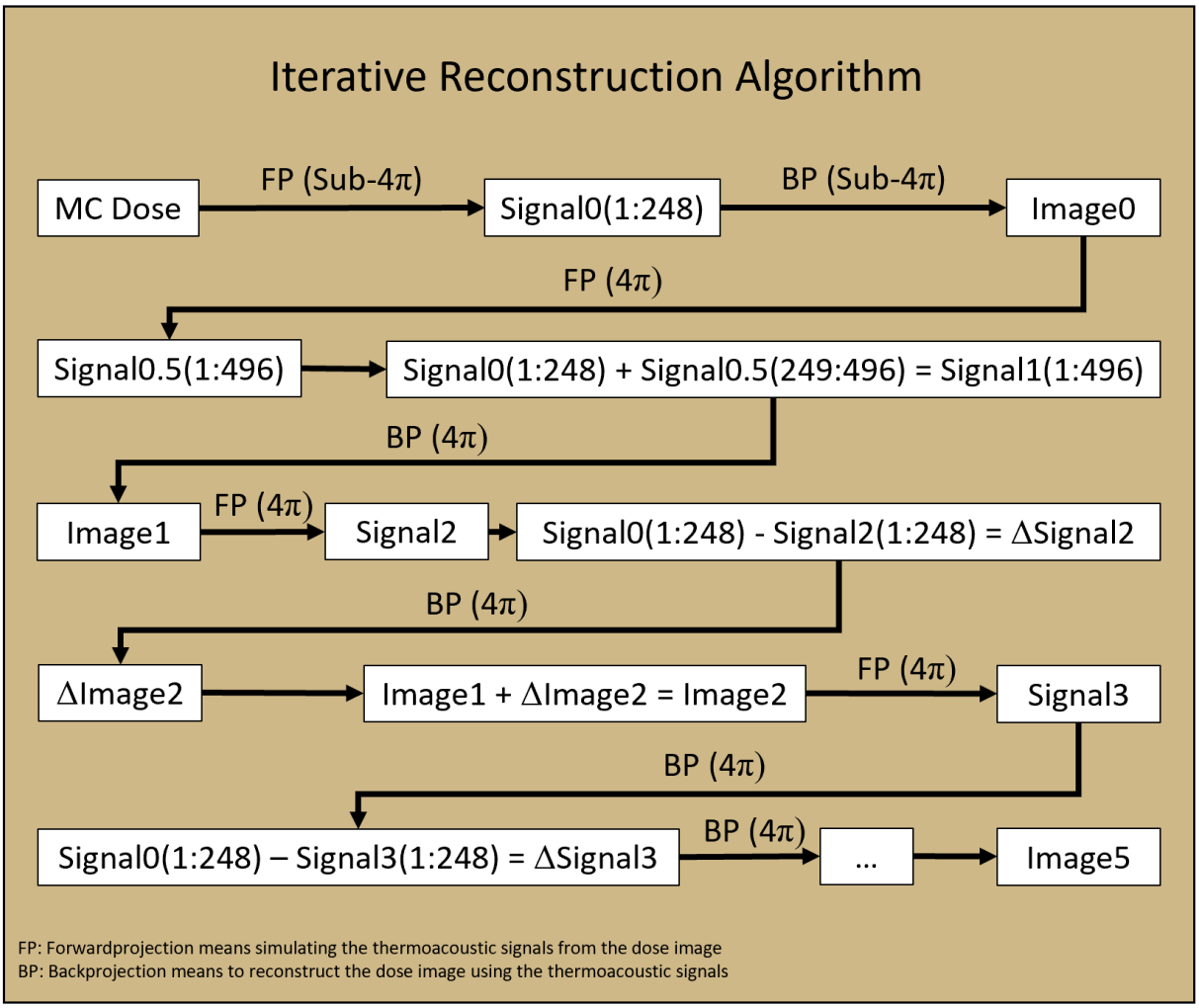

Figure 19: Iterative reconstruction schematic. Note that FP, forwardprojection, means to simulate thermoacoustic signals, and BP, backprojection, means to reconstruct an image from the signals. The indices, (1:248) for example, refer to the signal from transducers 1 through 248. While the algorithm is generalizable, the indices in this figure correspond to the iterative algorithm applied to NEXUS248; the transducers need to be aligned differently for NEXUS128. The indices for the 4π detector in this figure correspond to NEXUS496, which can be used for both NEXUS248 and NEXUS128.

First, the MC dose is imaged with a sub-4π detector (NEXUS128 or NEXUS248) and the thermoacoustic signal, Signal0, is acquired. Since the MC dose is representative of the physical dose, Signal0 is representative of the physically measured signals. Image0 is then reconstructed with Signal0 (note that this is the framework that has been used throughout this thesis prior to this point). The calibration constant of 2.2812×10^{-5} Gy/reconstruction intensity unit (see Section 3.3 Methods, Figure 8) is applied to the reconstruction image in each iteration, which is essential to achieving convergence to the MC dose. Thermoacoustic signals, Signal0.5, are then simulated

from the first reconstruction image, Image0, as would be measured by the 4π detector NEXUS496. Instead of using Signal0.5 (which is an intermediate step, denoted by 0.5) to simulate the next image, Signal0 is used for the transducers that exist in the sub-4π transducer arrays since those signals are the true signals. Combining Signal0 and Signal0.5 as described results in Signal1, which is then used to reconstruct an image, Image1, using NEXUS496. Image0 represents the initial sub-4π image reconstruction while Image1 represents the initial 4π image reconstruction. Although the missing projections have been filled in at this point, they are not necessarily the signals that would have actually been measured if physical transducers were in those positions to measure them. If the missing projections are correct, then they should produce signals equivalent to the measured signals, Signal0, which are the ground truth. Signal2 is simulated from Image1, and taking the difference Signal0 – Signal2 *for the transducers that exist in the sub-4π detector* shows how much the simulated signals are different from the measured signals, resulting in ΔSignal2. ΔSignal2 contains the information of how the filled-in "missing" projections need to change, and so these signals are used in the filtered backprojection algorithm to get ΔImage2, which represents how much the image (dose) needs to change. ΔImage2 is added to Image1 to achieve the updated Image2. While this updates the dose image to be closer to the MC dose, it takes several iterations of this before the reconstruction image dose converges to the MC dose. For the purposes of this study, 5 iterations were enough to achieve convergence.

6.2.3 Experiments

The iterative reconstruction algorithm was applied to both NEXUS248 and NEXUS128. Based on the results of Specific Aim 1, NEXUS248, with 2π angular coverage, can have the water level centered at isocenter because 2π coverage results in an image that has enough resemblance to the MC dose, eliminating the need to shift the water level off isocenter and introduce off-isocenter inaccuracies. NEXUS128, on the other hand, was chosen to have a water level shift of 40 mm because the "spike" artifact was eliminated at this water level. Because the information for the spike artifact is contained in the initial signals, which are used as the ground truth, the iterative reconstruction algorithm will assume that it is true signal and iteratively augment the spike. Thus, it is necessary that the water level be shifted in NEXUS128 in order to achieve convergence to the MC dose. This does, however, introduce the potential for off-isocenter blurring.

6.3 Results

The iterative reconstruction algorithm was applied to the reconstruction images from NEXUS248 and NEXUS128. Figure 20 shows 2D slices (of the 3D images) for NEXUS248 from iterations 0 through 5. Figure 21 shows the depth dose including dose magnitude (left) of the reconstruction images, as well as the PDDs for iteration 0 and 5 compared to the MC PDD (right). Figure 22 shows the same information as Figure 21 but for the lateral profile at the depth of the Bragg peak. Figure 23, Figure 24, and Figure 25 respectively show the same information as Figure 20, Figure 21, and Figure 22 but for NEXUS128.

6.3.1 NEXUS248 Iterative Reconstruction Results

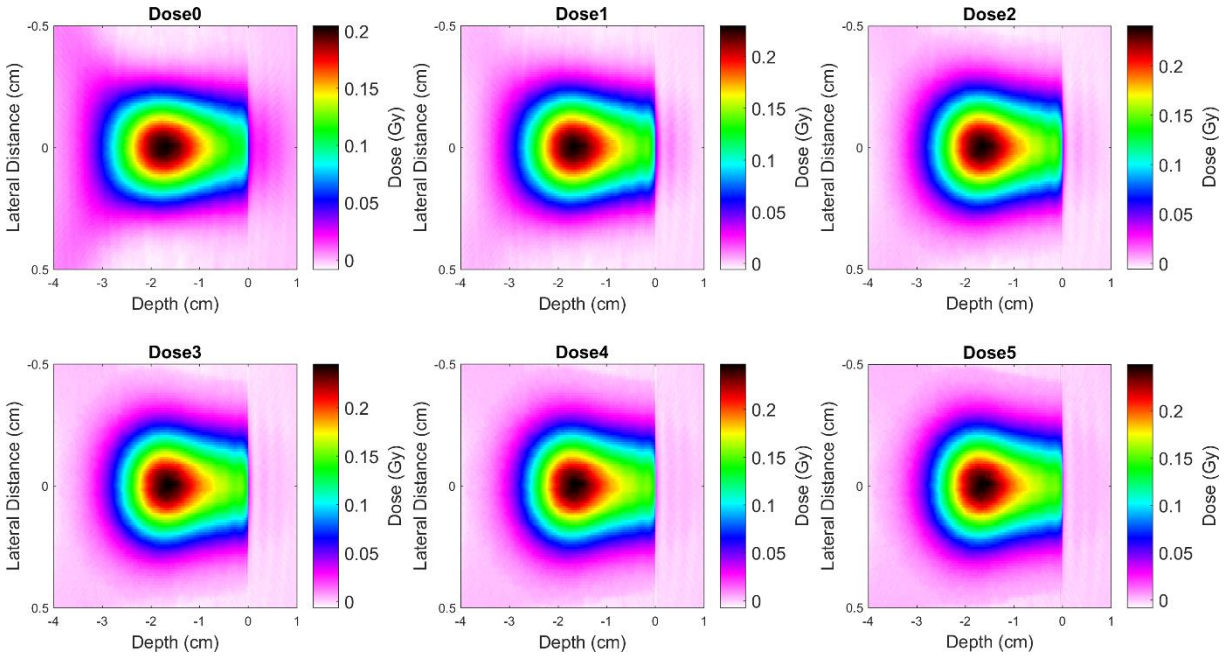

Figure 20: NEXUS248 iterative image reconstruction. 2D slices (of 3D images) of the iteratively reconstructed dose from iteration 0 to iteration 5.

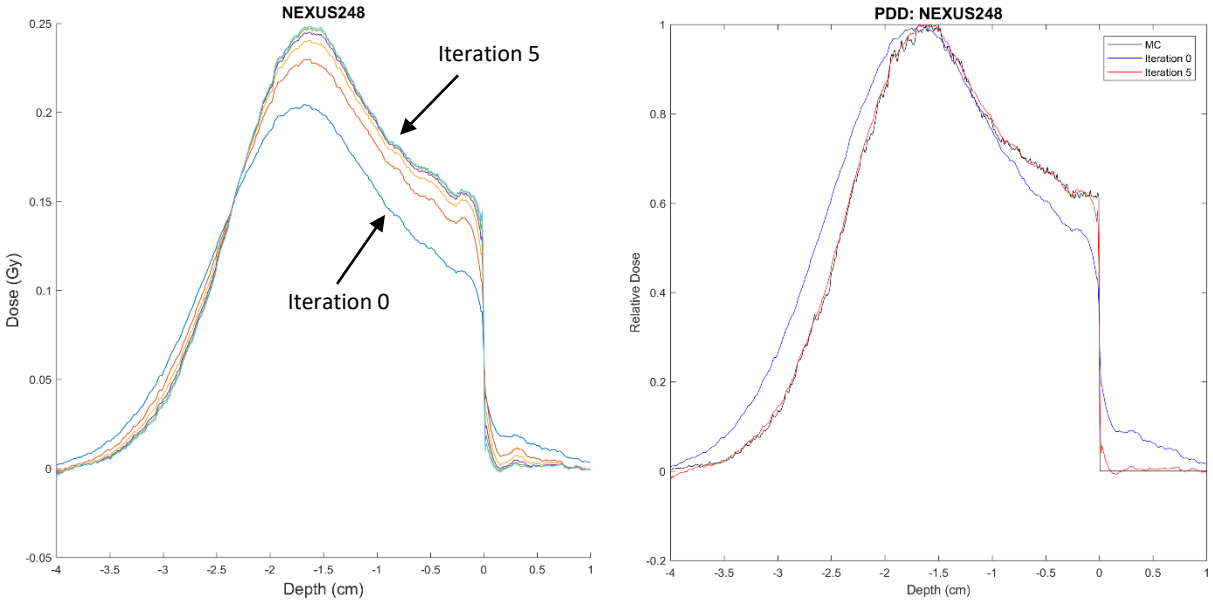

Figure 21: NEXUS248 iterative image reconstruction. Left: Depth dose. Note the convergence of the iterations to the level of the MC dose (≈ 0.25 Gy). Right: PDD. Note how the iteration 5 dose agrees with the MC dose significantly better than the iteration 0 dose does.

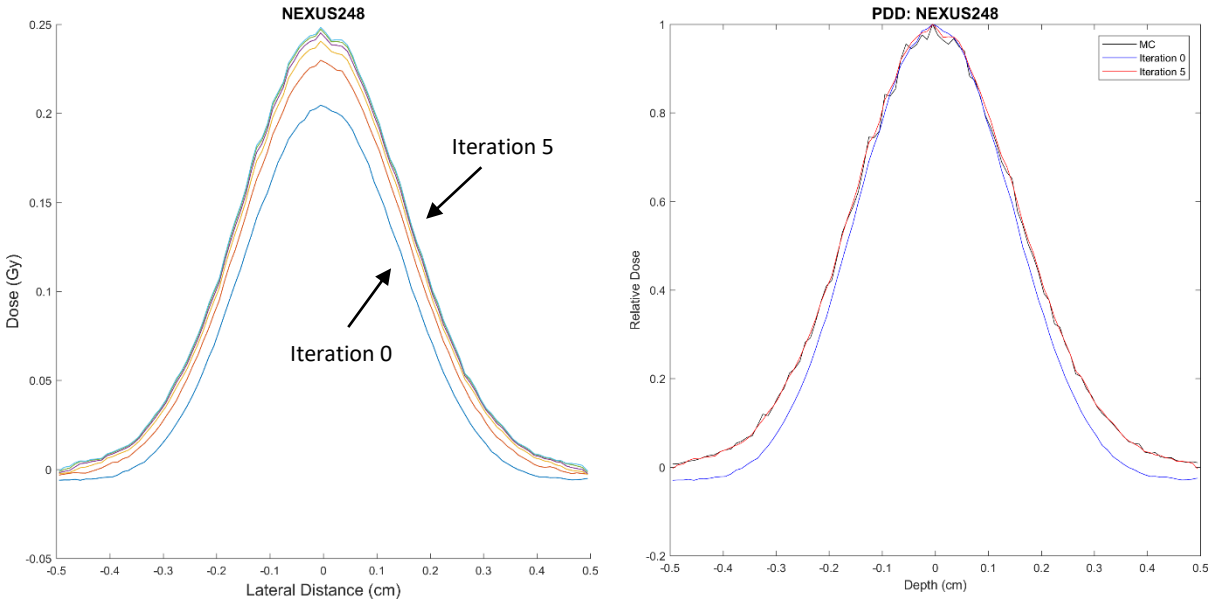

Figure 22: NEXUS248 iterative image reconstruction. Left: Lateral dose. Note the convergence of the iterations to the level of the MC dose (≈ 0.25 Gy). Right: Percent lateral dose. Note how the iteration 5 dose agrees with the MC dose significantly better than the iteration 0 dose does.

6.3.2 NEXUS128 Iterative Reconstruction Results

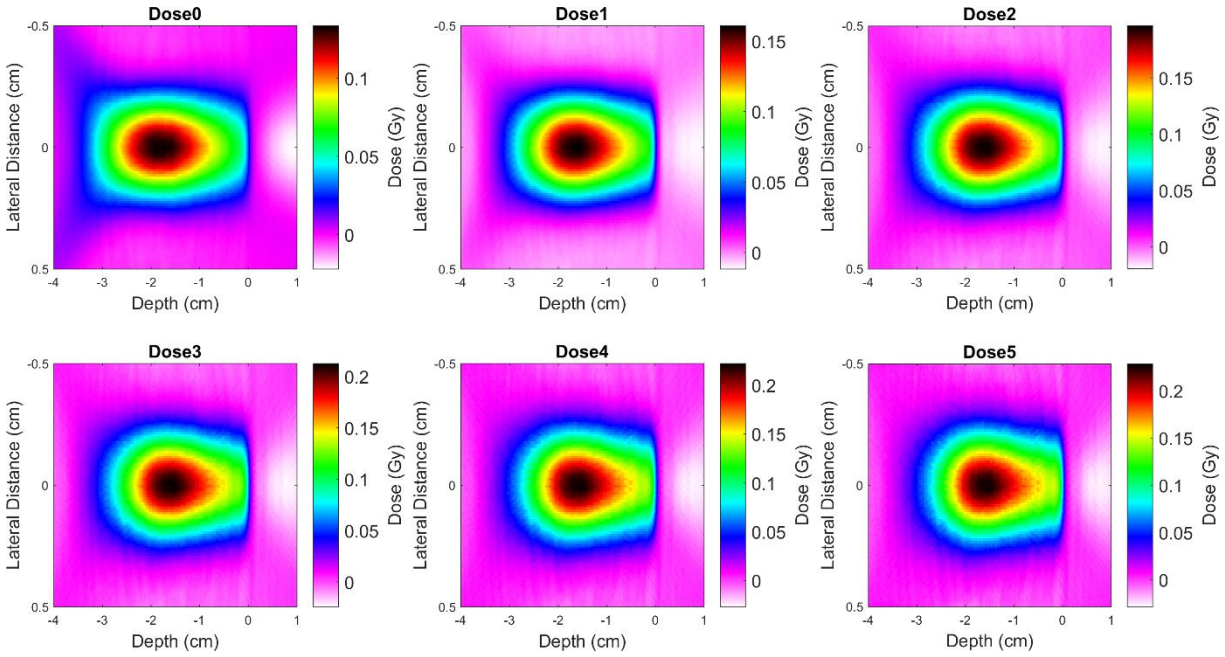

Figure 23: NEXUS128 with 40 mm water level shift iterative image reconstruction. 2D slices (of 3D images) of the iteratively reconstructed dose from iteration 0 to iteration 5.

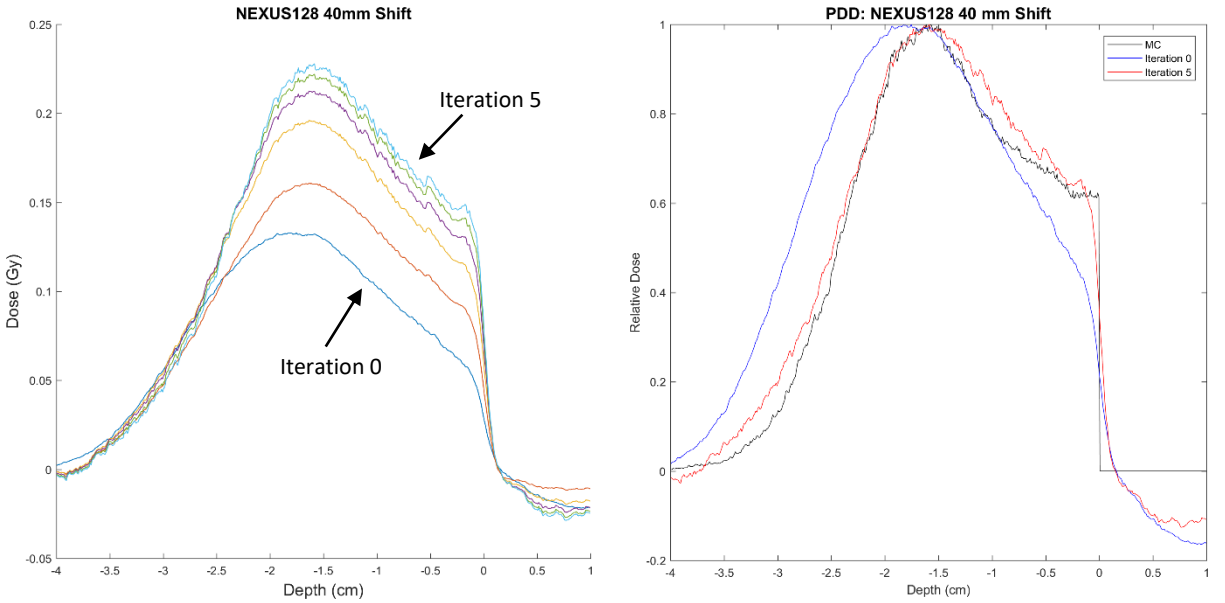

Figure 24: NEXUS128 with 40 mm water level shift iterative image reconstruction. Left: Depth dose. Note that while the iterations converge, the level of the MC dose (≈ 0.25 Gy) is not reached. Right: PDD. Note how the iteration 5 dose agrees with the MC dose significantly better than the iteration 0 dose does. Although iteration 5 more closely matches the MC dose, the agreement is less strong than for NEXUS248 (Figure 21) due to being off isocenter.

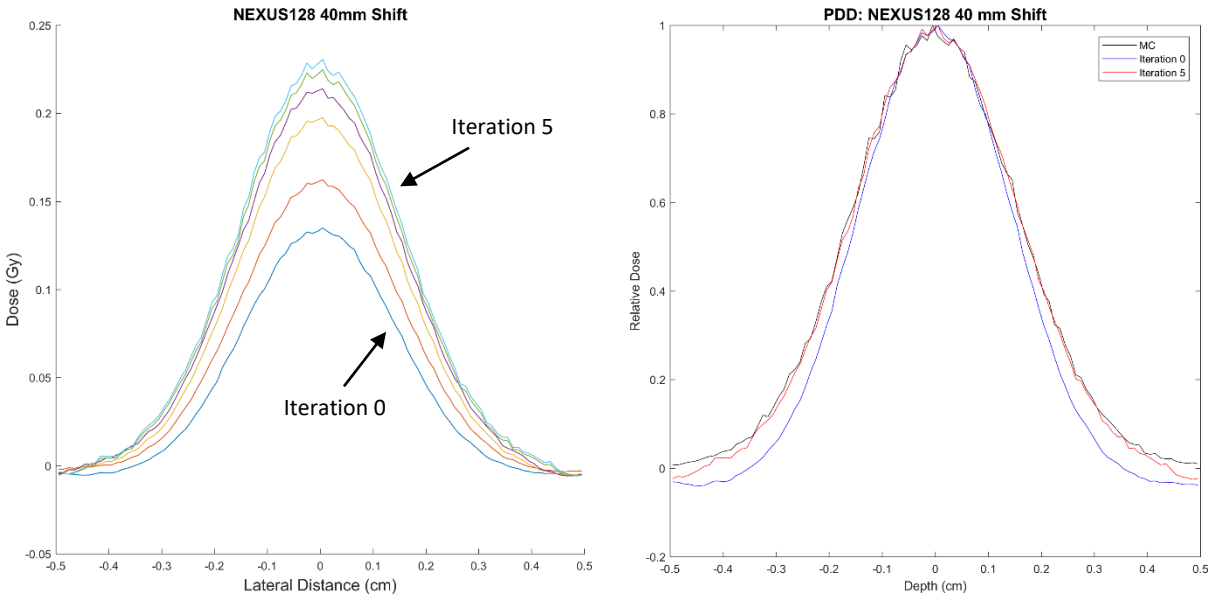

Figure 25: NEXUS128 with 40 mm water level shift iterative image reconstruction. Left: Lateral dose. Note that while the iterations converge, the level of the MC dose (≈ 0.25 Gy) is not reached. Right: Percent lateral dose. Note how the iteration 5 dose agrees with the MC dose significantly better than the iteration 0 dose does. Although iteration 5 more closely matches the MC dose, the agreement is less strong than for NEXUS248 (Figure 22) due to being off isocenter.

6.4 Discussion

As shown in Figure 20, Figure 21, and Figure 22, the iterative reconstruction algorithm was able to achieve convergence to the MC dose for NEXUS248. In Figure 21 and Figure 22, left, the initial dose from iteration 0 shows that the spatial distribution and magnitude of the dose are inaccurate to the MC dose. With each increasing iteration, the spatial distribution changed and the magnitude increased to be closer to the MC dose. By the last several iterations, there is little difference between successive iterations, demonstrating convergence. The magnitude of the dose in iteration 5 reaches ≈ 0.25 Gy, which is the magnitude of the MC dose. Looking at the PDD to highlight the spatial distribution without magnitude differences, Figure 21 and Figure 22, right, show how accurate the iteration 0 and iteration 5 PDDs are to the MC PDD. While iteration 0 is a decent image overall, there is significant deviation from the MC dose, but the convergence in iteration 5 achieved a near perfect match to the MC PDD, just as KMS256 demonstrated was possible for a 4π detector in Specific Aim 1. Thus, using the iterative reconstruction algorithm with NEXUS248, a 2π detector, a near perfect image of the dose both in magnitude and spatial distribution was achieved.

Figure 23, Figure 24, and Figure 25 show similar results for NEXUS128 with a 40 mm water level shift. While the spatial distribution of the dose changed and dose magnitude increased with each iteration (Figure 24 and Figure 25, left) as was the case for NEXUS248, it was not able to achieve convergence to the MC dose, even though a lesser level of convergence is evident. The convergence dose magnitude is roughly 0.025 Gy (2.5 cGy) or 10% short of the MC dose. In Figure 24 and Figure 25, right, the PDD agreement with the MC PDD significantly increased from iteration 0 to iteration 5, although the image is not near perfect. There is some discrepancy between the iteration 5 and MC PDDs at the distal edge and entrance dose in Figure 24 (right) (note that while there is a "dip" in dose to the right of 0 cm depth, it is likely inconsequential as this is not within the water phantom), and there is deviation for larger lateral distances (Figure 25, right). This is due to being off-isocenter, as off-isocenter blurring effects are present in the initial (ground truth) measured signals and will be augmented through the iterative reconstruction algorithm. These results highlight the need for sufficient baseline angular coverage so that the dose does not have to be moved off-isocenter.

With enough said about the discrepancy between the MC dose and iteration 5 dose for NEXUS128, it is important to highlight the dramatic image accuracy improvement between the initial NEXUS128 image on-isocenter (Figure 12, left) and the iteration 5 dose with a 40 mm shift. The initial on-isocenter image showed poor resemblance to the MC dose, having almost no agreement in the PDDs, as well as having a large "spike" artifact, and improved to having an iteration 5 dose that is arguably better than the NEXUS248 iteration 0 dose (compare Figure 24 to Figure 21 and Figure 25 to Figure 22). While a near perfect image may be beyond the capabilities of NEXUS128, with the correct setup and reconstruction algorithm, it can produce images that may potentially be acceptable depending on the application. Furthermore, the "decent" iteration 0 dose for NEXUS248 was improved to a near perfect image in iteration 5. While Specific Aim 1 found a 2π detector to be able to produce decent images potentially useful in some applications and found a sub-2π detector to produce inadequate images, the application of the iterative reconstruction algorithm was able to improve 2π images from decent to near perfect and sub-2π images from inadequate to decent. Thus, these results demonstrate that a 4π detector is not required to produce useful images, but that sub-4π detectors with the investigated geometries can be used to provide images of proton beams with LPA characteristics (e.g., wide energy spreads, angular divergence) that may potentially have sufficient accuracy.

6.5 Conclusion

An iterative reconstruction algorithm was applied to MC dose images from NEXUS248 and NEXUS128 with a 40 mm water level shift was able to improve image accuracy. The iterative reconstruction algorithm was able to take a decent NEXUS248 initial image and improve it to a near perfect image of the MC dose. The image from NEXUS128 was able to be improved from an inadequate image to a decent, potentially useful image, although a near perfect image was not able to be achieved due to off-isocenter blurring. In contrast to the results in Specific Aim 1, these results in Specific Aim 2 show that a 4π detector is not required to produce images with sufficient accuracy, but that detectors with 2π and possibly less angular coverage may be able to produce sufficiently accurate images. The inability to achieve a near perfect image using NEXUS128 with a 40 mm water level shift demonstrates the need for sufficient baseline angular coverage in order to image the dose on-isocenter and eliminate off-isocenter blurring effects.

CHAPTER 7. SPECIFIC AIM 3

7.1 Introduction

7.1.1 Noisy Signals

Specific Aims 1 and 2 have demonstrated the feasibility of accurately reconstructing dose from proton beams with LPA characteristics in ideal, theoretical settings. In real settings, noise is present and affects thermoacoustic signal detection. If the signal is less than or similar to background noise, the noise will mask the signal, so for a given amount of noise (e.g., acoustic or electronic noise) the signal must have a certain intensity or greater for the dose to be seen in an image. The sensitivity of the detector is the minimum dose needed to achieve a specific endpoint (e.g., the minimum detectable dose, 1 mm range uncertainty, etc.), with the magnitude of the dose being dependent on the number of protons per pulse. As mentioned earlier in Section 2.1, studies have shown that LPA proton beams can be achieved with 10^7-10^{12} of protons per pulse,[5,9–11] and the beam modeled in this thesis with 10^7 protons per pulse results in a Bragg peak dose of ≈ 0.25 Gy. By adjusting the noise level in the signals, the sensitivity of the detector for a given endpoint can be determined by finding the lowest noise level that achieves the endpoint. In Specific Aim 3, different noise levels are applied to the thermoacoustic signals to determine the detector sensitivity.

7.1.2 Frequency Dependence

Determining the detector sensitivity is not as straight forward as just adding noise since both the thermoacoustic signals and noise are frequency dependent. As mentioned in Section 2.2.2, the transducers in the transducer array have a bandwidth (measured by impulse response), having a center frequency of 5 MHz. To correct for the differential sensitivity of signal detection at different frequencies, the impulse response is deconvolved from the measured signals, as described in Eq. 17. Doing this amplifies the frequencies with less detection sensitivity so that the frequencies from the signal are equally sampled. In the absence of noise in Specific Aims 1 and 2, this correction works perfectly (the results from these aims are exactly the same for theoretical signals (no impulse response convolution or a delta-function impulse response) and for impulse response convolved signals with impulse response deconvolution). However, with noise present, the signal-

to-noise ratio may be too low to get useful information from these frequencies, while the impulse response deconvolution amplifies noise in addition to the signal. The image reconstruction quality therefore depends on what the signal frequencies are. As discussed in Section 3.1.3, the wide energy spread of the LPA proton beam model results in lower frequency signals. The frequency spectrum for the theoretical signal shown in Figure 5 (left) is compared to the measured impulse response frequency spectrum shown in Figure 26 (left), and the theoretical signal frequency spectrum is compared to the impulse response convolved signal frequency spectrum (right). As can be seen, the thermoacoustic signal mainly has frequencies lower than the transducer center frequency, which results in a reduced signal intensity at these frequencies. Figure 27 shows how the impulse response deconvolution amplifies both the signal and the noise significantly at these frequencies. While the effects of the transducer bandwidth are unavoidable, an apodizing function can be applied and fine-tuned to filter the high frequency noise while maintaining the low frequencies from the thermoacoustic signal, which significantly improves image quality in the presence of noise.

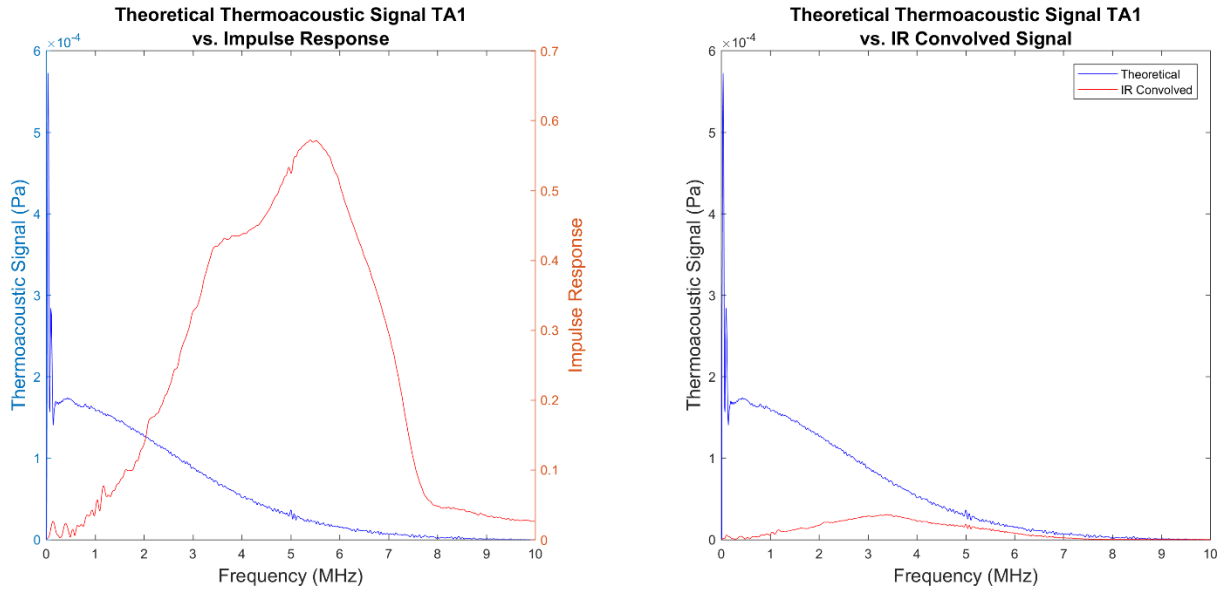

Figure 26: (Left) Comparison of impulse response (red) to example thermoacoustic signal frequency spectrum. Note that the center frequency of the impulse response (5 MHz) is higher than the majority of the signal frequency, which when convolved together greatly diminishes the signal (right).

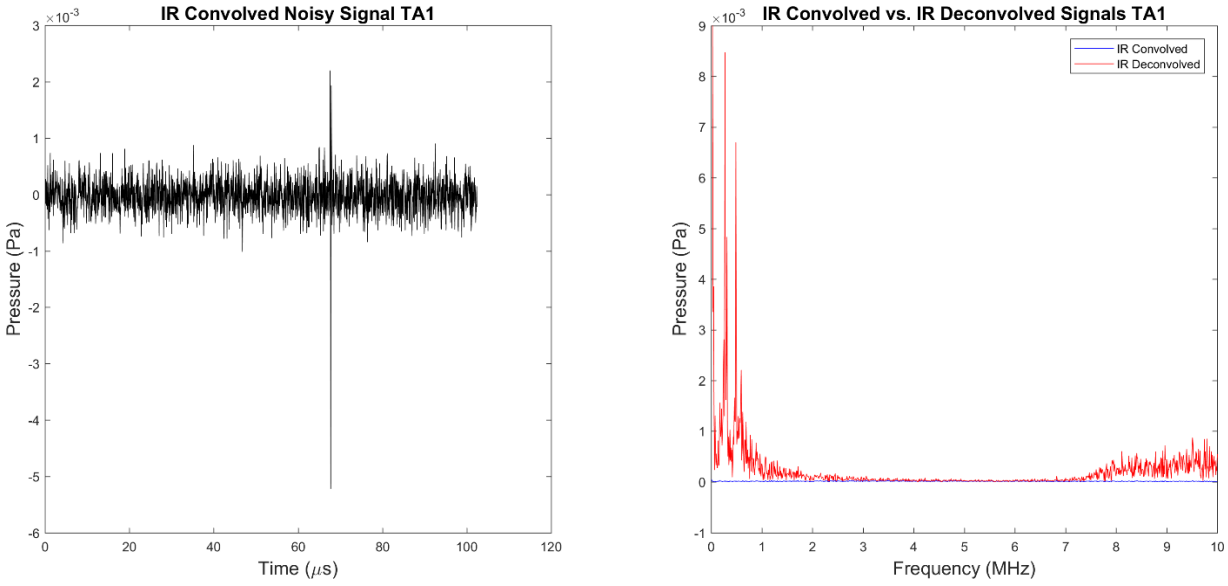

Figure 27: (Left) The same signal from Figure 26 with impulse response convolution is shown with added noise (0.5% of 57 mPa, which is the maximum pressure amplitude from all non-impulse response convolved signals). (Right) The blue line is the frequency spectrum for the noisy signal shown in the left figure, and the red signal is the signal after impulse response deconvolution. Notice how noise is greatly amplified in addition to the signal, so much that the impulse response convolved signal (blue) appears as a flat line in comparison.

7.2 Methods

The thermoacoustic waves were simulated from the MC dose. Both the theoretical signals and impulse response convolved signals were calculated in order to investigate the bandwidth dependent sensitivities. Different levels of Gaussian noise with a mean of 0 and standard deviation of 1, scaled by the noise level, were added to the theoretical signals and the post-impulse response convolved signals. The levels of noise were defined as a fraction of the maximum compression (positive) signal amplitude from the theoretical signals over all the transducers and rotation angles. It should be noted the reference maximum signal amplitude excluded the signal (spike in the signal) from the water edge. Figure 28 shows that maximum signal amplitude, selected as described above, with a peak compression pressure of 0.057 Pa = 57 mPa.

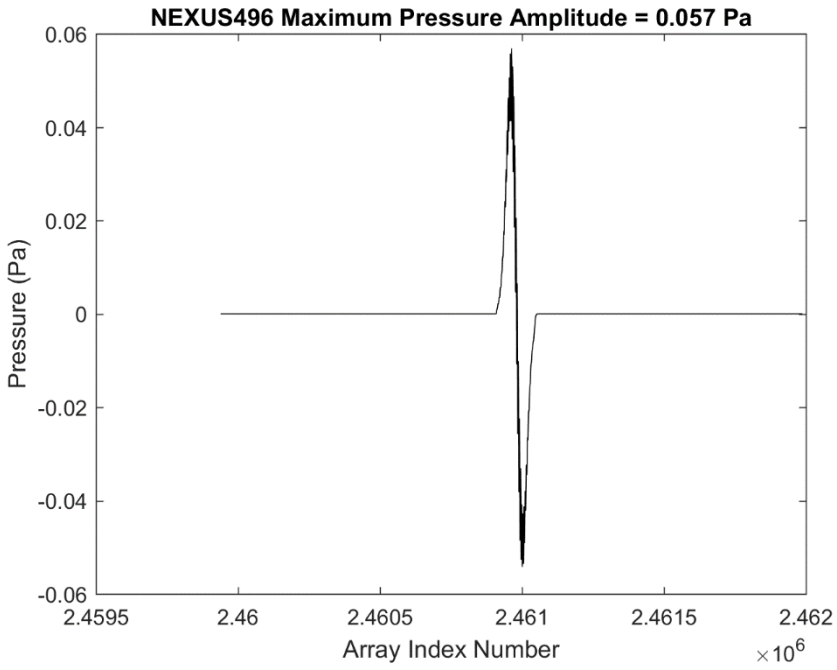

Figure 28: Signal with maximum compression pressure. Note that the x-axis shows the array index number instead of time or acquisition number since the index of the peak pressure could be found but not the index of the start of the acquisition for this signal.

Table 1 shows the levels of noise added to the impulse response convolved signals, and Table 2 shows the levels of noise added to the theoretical signals, which were larger due to greater sensitivity.

Table 1: Noise levels added to the post-impulse response convolved signals. The percent noise is relative to 57 mPa, which is the maximum compression signal amplitude (excluding signals from the water edge). The noise distribution is Gaussian with a mean of 0 and standard deviation of 1, scaled by the noise factor.

Percent Noise	0.5%	1%	2%	3%	4%
Absolute Pressure (mPa)	0.285	0.57	1.14	1.17	2.28
Percent Noise	5%	6%	7%	10%	
Absolute Pressure (mPa)	2.85	3.42	3.99	5.7	

Table 2: Noise levels added to the theoretical signals. The percent noise is relative to 57 mPa, which is the maximum compression signal amplitude (excluding signals from the water edge). The noise distribution is Gaussian with a mean of 0 and standard deviation of 1, scaled by the noise factor.

Percent Noise	0.5%	10%	25%	50%	75%
Absolute Pressure (mPa)	0.285	5.7	14.25	28.5	42.75
Percent Noise	100%	150%	275%		
Absolute Pressure (mPa)	57	85.5	156.75		

The filter function used in the filtered back projection algorithm included a cosine apodizing function, which was used to filter higher frequency noise (note that the noise spans the entire frequency distribution):

$$A(\omega) = \frac{1}{2}\left(1 + \cos\left(\frac{\pi\omega}{\omega_0}\right)\right), \quad \text{Eq. 20}$$

where $A(\omega)$ is the apodizing function, ω is the frequency, and ω_0 is the center frequency. Not shown in Eq. 20 is the cutoff frequency ω_c, above which all higher frequencies are set to zero amplitude. The parameters ω_0 and ω_c can be fined tuned and were both chosen to be 5 MHz in order to filter out high frequency noise, without affecting the thermoacoustic signal (see Figure 26 and Figure 27). Figure 29 shows the filter function (see Eq. 18), including a ramp function of $\pi\omega$ but *excluding the impulse response deconvolution* for purpose of clarity in this figure (the impulse response deconvolution was used in the simulations).

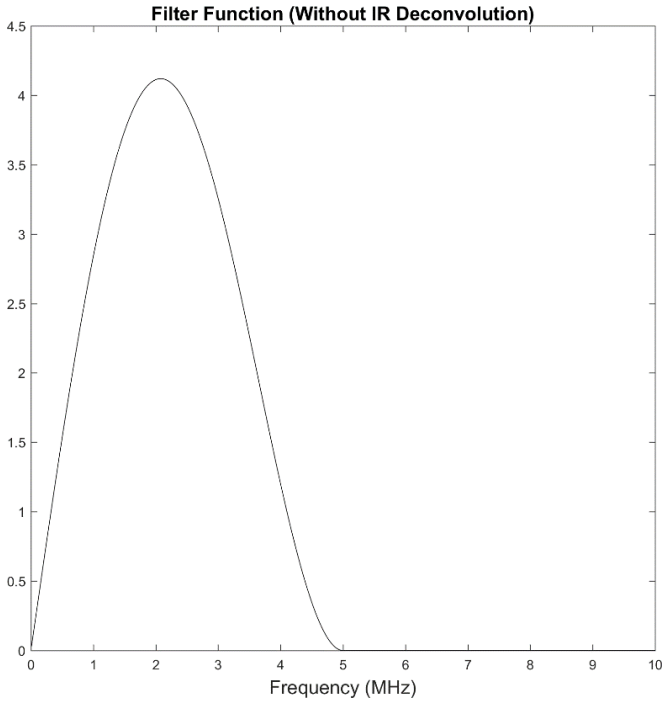

Figure 29: Filter function including ramp and apodizing functions but excluding impulse response deconvolution (for figure clarity). The impulse response deconvolution was used in the simulations.

Image reconstruction was then performed using the filtered signals with the NEXUS496 design. To evaluate the influence of noise, the MC dose was subtracted from the dose obtained from the reconstruction image to get the voxel-wise residuals, and a Gaussian curve was fit to a histogram of the residuals to determine the mean and standard deviation of the residuals distribution. The systematic error was calculated as

$$\text{systematic error} = \frac{\mu_{res}}{D_{Bragg}} \times 100\% \qquad \text{Eq. 21}$$

where μ_{res} is the mean of the residuals distribution and D_{Bragg} is the MC Bragg peak dose. The systematic error describes the offset of the reconstruction image dose from the MC dose, relative to the Bragg peak dose; at 100% systematic error, the offset is as large as the magnitude of the Bragg peak. Ideally, there would be no systematic offset regardless of noise level, but since the noise is part of the signal that is backprojected, it can affect the magnitude of the reconstructed dose. The systematic error was evaluated as a function of noise level; the figure of merit used is for the systematic error to be less than 5%, which is a common criterion for dosimetric accuracy.

The statistical error was determined from the following equation:

$$\text{statistical error} = \frac{\text{FWHM}_{res}}{D_{Bragg}} \times 100\%, \qquad \text{Eq. 22}$$

where FWHM_{res} is the full-width half-maximum of the residuals. FWHM_{res} is a measure of the spread of the residuals with units of dose, so the statistical error is a measure of this spread relative to the Bragg peak dose; at 100% statistical error, the spread of the residuals has as great a magnitude as the Bragg peak. The statistical error was evaluated as a function of noise level and a linear model was fit to the data.

The sensitivity was evaluated for three therapeutic endpoints: 2 Gy fraction commonly used in standard radiation therapy, 10 Gy fraction for radioimmunotherapy, and minimum dose sensitivity of the detectors (the ability to observe a dose above 3 standard deviations of noise for 99.7% confidence). Clinically, the dose for 2 Gy fractions should have less than 2% statistical error; for radioimmunotherapy, the dose should be within 5% statistical error; to see dose above 3 standard deviations of noise, the statistical error should be within 78.5%. Using the linear model from the statistical error data, these criteria were used to calculate the corresponding noise levels. The previous study in our lab by Alsanea et al. calculated the absolute noise of a hydrophone with 0.4 MHz bandwidth and an RTI of 50 dB re 1 μPa/√Hz to be 63 mPa.[20] To facilitate a rough comparison, the transducers in NEXUS496 were assumed to also have an absolute noise of 63 mPa at the center frequency (5MHz). To calculate the pressure sensitivity for these transducers, which is the smallest maximum compression pressure that can be detected with 63 mPa noise (i.e., for the maximum compression pressure signal amplitude, such as in Figure 28, the smallest amplitude this signal could be and able to be detected according to the noise level criteria), the maximum signal pressure ($p_{sig,sim}$) and absolute noise ($p_{noise,sim}$) from the simulated signals were related to the maximum signal pressure ($p_{sig,TA}$) and absolute noise ($p_{noise,TA}$) of the transducers through the noise level:

$$\frac{p_{noise,sim}}{p_{sig,sim}} = \text{noise level} = \frac{p_{noise,TA}}{p_{sig,TA}} \qquad \text{Eq. 23}$$

where $p_{noise,TA}$ = 63 mPa and $p_{sig,TA}$ is defined as the pressure sensitivity of the transducers. Eq. 23 shows how the noise level chosen from the simulated results according to the sensitivity criteria

(i.e., the 2%, 5%, and 78.5% statistical error criteria) can be used to calculate the transducer pressure sensitivity, which is calculated as

$$p_{sig,TA} \equiv p_{sensitivity} = \frac{63 \text{ mPa}}{\text{noise level}} \quad \text{Eq. 24}$$

Given $p_{sensitivity}$, a calibration curve (Figure 30) can be used to determine the dose sensitivity. The calibration curve was created by measuring the maximum (non-noisy) theoretical pressure signal amplitude (which was the same signal in Figure 28) and comparing it to the MC Bragg peak dose for varying amounts of protons/pulse. The calibration was determined to be

$$\text{Dose} = 4.4451 \cdot p_{sensitivity} - 5.101 \times 10^{-4}. \quad \text{Eq. 25}$$

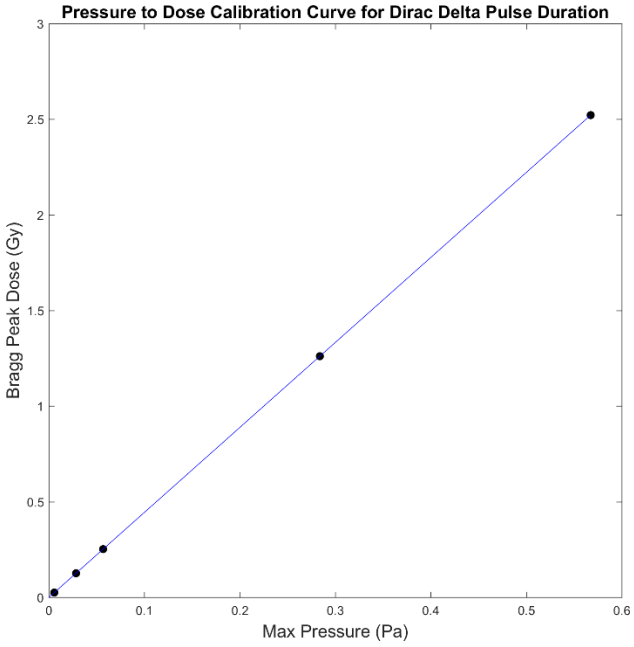

Figure 30: Pressure to dose calibration curve. The pressure is from the non-noisy, theoretical maximum signal amplitude, and the dose is from the MC Bragg peak. Measurements were taken for 1×10^6, 5×10^6, 1×10^7, 5×10^7 and 1×10^8 protons/pulse. The linearity between maximum pressure signal amplitude and Bragg peak dose is strong, although the number of protons/pulse and maximum pressure signal amplitude are non-linearly related. The calibration curve was determined to be $\text{Dose} = 4.4451 \cdot p_{sensitivity} - 5.101 \times 10^{-4}$ with a correlation coefficient of $r = 1.0$.

7.3 Results

The levels of noise described in

Table 1 and Table 2 were added to the post-impulse response convolved and theoretical thermoacoustic signals, respectively. The signals were filtered and reconstructed using NEXUS496. Figure 31 and Figure 32 show the 2D image slices reconstructed using the impulse response convolved and theoretical signals, respectively, for each noise level.

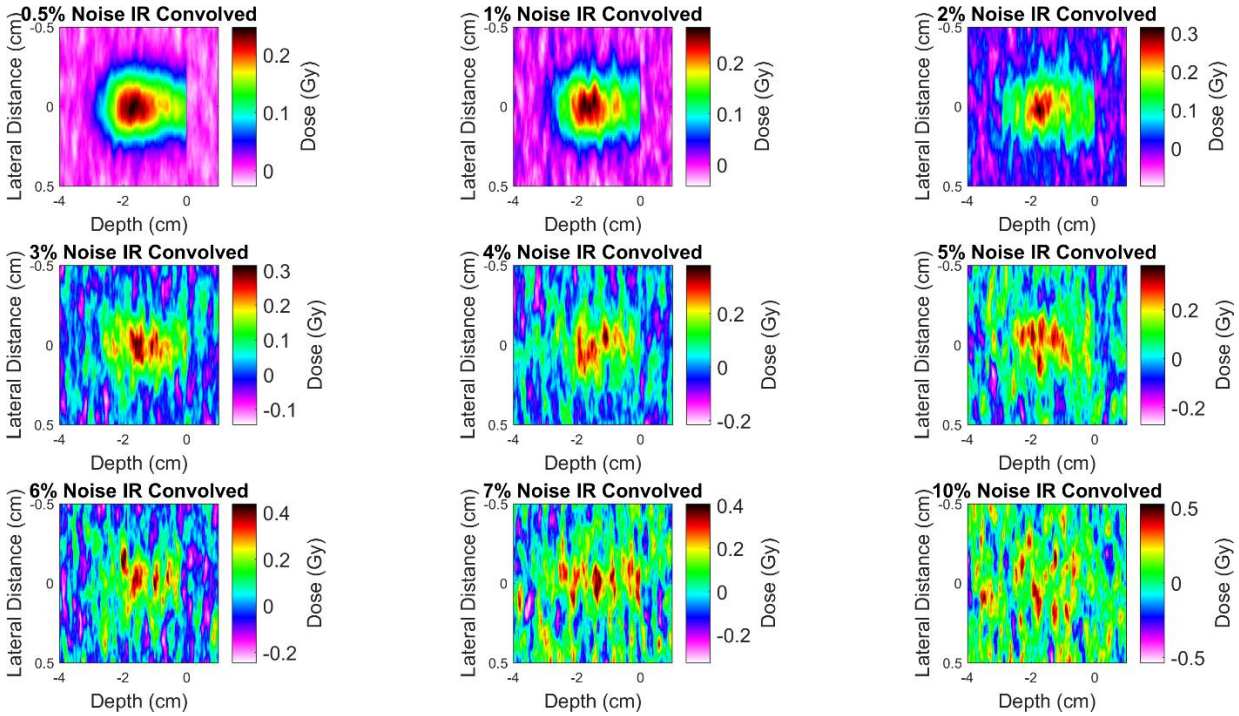

Figure 31: Noisy images reconstructed with impulse response convolved signals. Note that the distorted look of the images is due to the presence of low-frequency noise that has been amplified by the impulse response deconvolution (see Figure 27, right) while high-frequency noise has been filtered out.

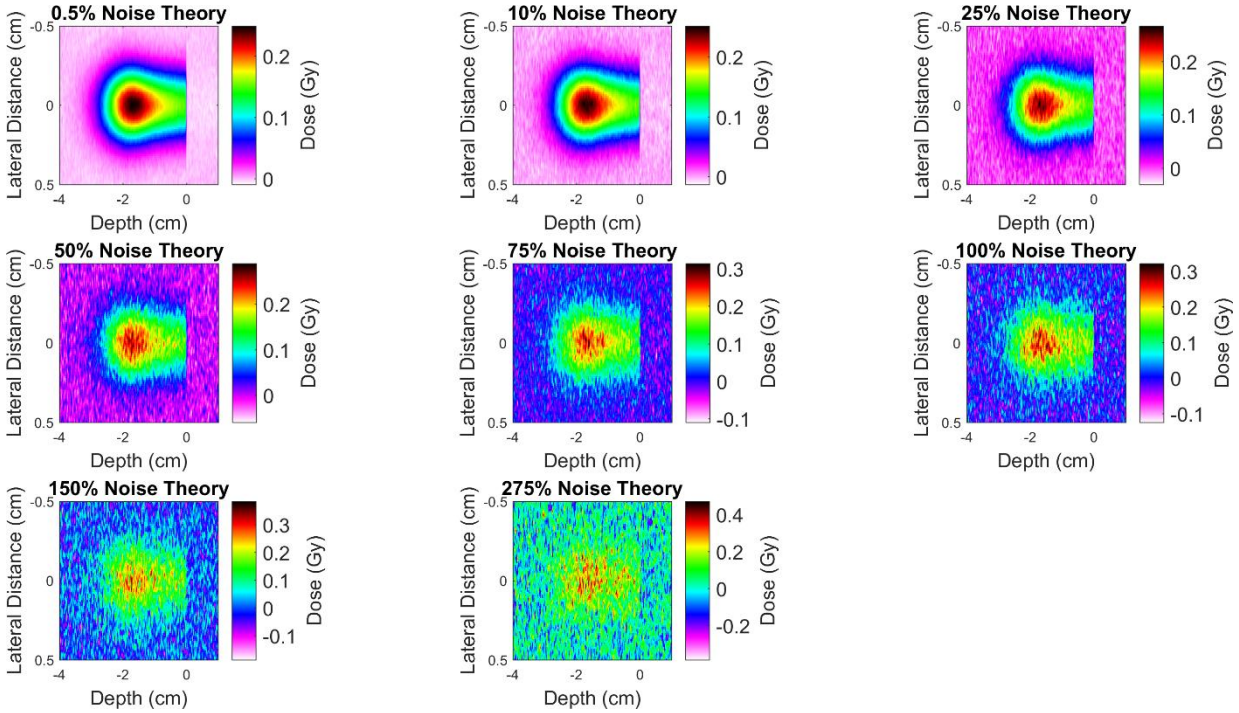

Figure 32: Noisy images reconstructed with theoretical signals. While the noise is still low frequency as it is in Figure 31, it is not amplified because there is no impulse response deconvolution, resulting in less distorted looking images.

Examples of histograms with fitted Gaussian curves are shown below in Figure 33 for 0.5% noise and 10% noise (for the impulse response convolved images).

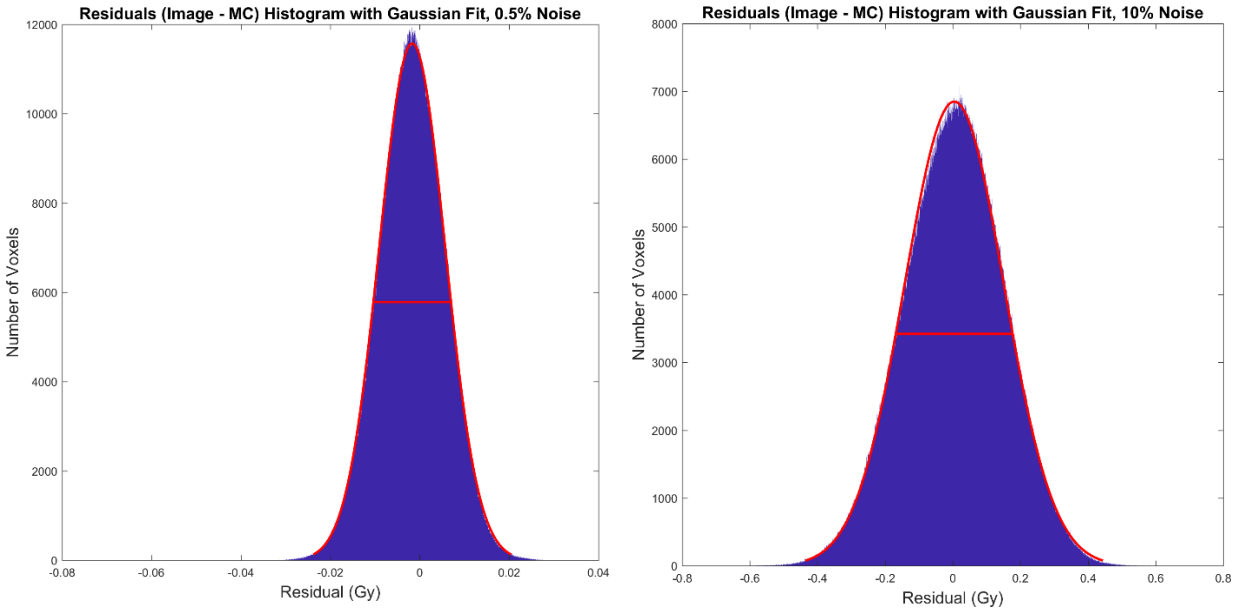

Figure 33: Example residual histograms (Image – MC) for 0.5% noise (left) and 10% noise (right). In blue are the histogram bins, and a red Gaussian curve is fit to the histogram. The red line going through the center is the FWHM. Note that the scaling is different between the two figures for clarity.

Figure 34 shows the systematic error as a function of noise for the impulse response (left) and theoretical (right) images, and Figure 35 shows the statistical error as a function of noise.

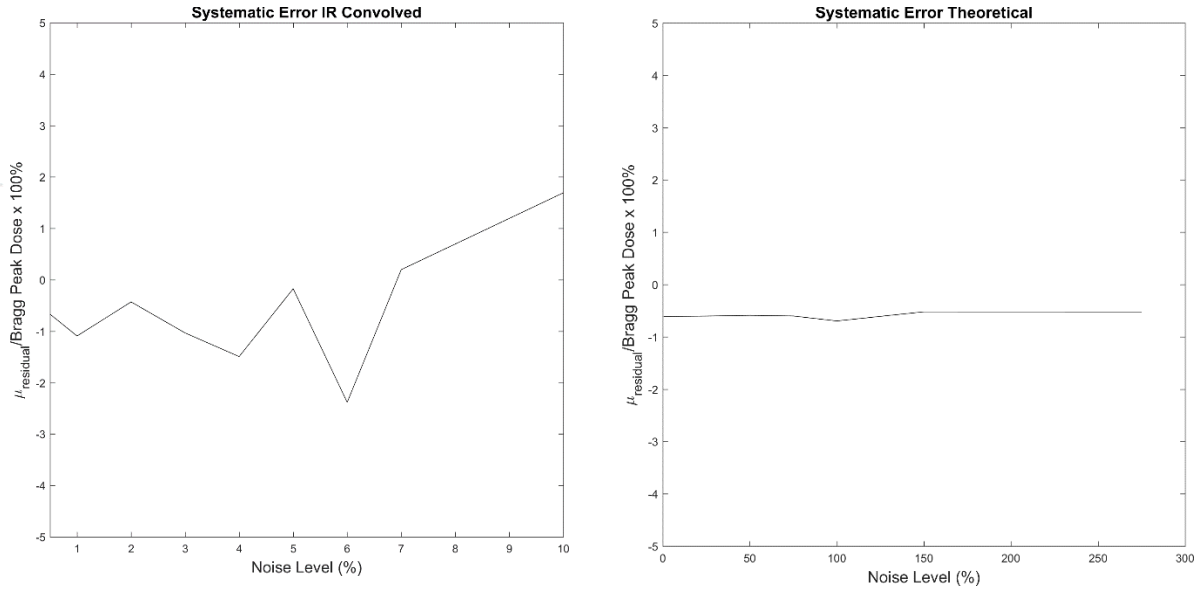

Figure 34: Systematic error for impulse response images (left) and theoretical images (right). Note that the systematic error lies within 5% for both images, although it is lower for the theoretical images.

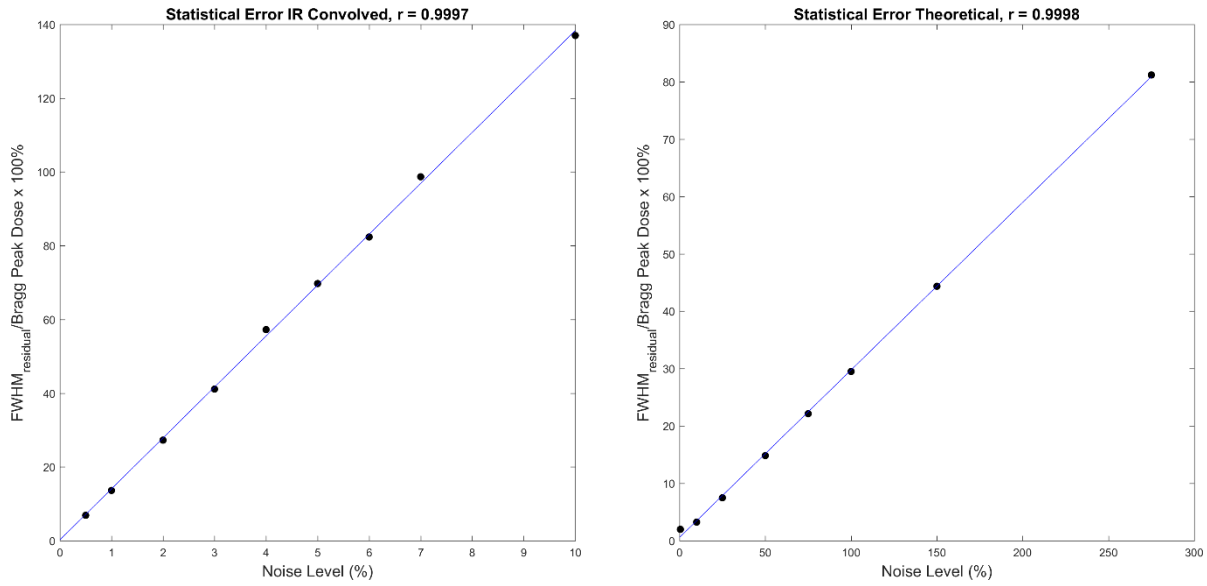

Figure 35: Statistical error for impulse response images (left) and theoretical images (right). Note the strong linearity with correlation coefficients of $r = 0.9997$ for the impulse response images and $r = 0.9998$ for the theoretical images. The impulse response linear model was determined to be $\text{statistical error} = 13.8127 \cdot \text{noise level}(\%) + 0.240$, and the theoretical linear model was determined to be $\text{statistical error} = 0.2921 \cdot \text{noise level}(\%) + 0.566$.

The impulse response linear model shown in Figure 35 was determined to be $\text{statistical error} = 13.8127 \cdot \text{noise level}(\%) + 0.240$, and the theoretical linear model was determined to be $\text{statistical error} = 0.2921 \cdot \text{noise level}(\%) + 0.566$. Using these linear models, the respective noise levels for the impulse response signals and theoretical signals to achieve 2% statistical error (2 Gy radiotherapy fractions) were determined to be 0.13% and 4.91%, the noise levels to achieve 5% statistical error (10 Gy radioimmunotherapy fractions) were determined to be 0.34% and 15.18%, and the noise levels for minimum dose sensitivity were determined to be 5.67% and 267%. Using Eq. 24, the impulse response and theoretical pressure sensitivities were respectively calculated to be 48.5 Pa and 1.283 Pa, 18.5 Pa and 0.415 Pa, and 1.1 Pa and 0.024 Pa for the three respective endpoints. Using Eq. 25, the dose sensitivities were respectively determined to be 216 Gy and 5.7 Gy, 82 Gy and 1.8 Gy, and 4.9 Gy and 0.1 Gy.

7.4 Discussion

The systematic error for the impulse response and theoretical images were both within 5% over all the investigated noise levels, demonstrating that the deviation of the image dose from the

MC dose is acceptably small up to sensitivity limits. It is important to monitor the systematic error since significant deviations from the MC dose could occur without a high statistical error conspicuously drawing attention to anything that may be wrong in the image.

The noise levels calculated for the three endpoints (2% statistical error for 2 Gy radiation therapy fractions, 5% statistical error for 10 Gy radioimmunotherapy fractions, and 78.5% statistical error for minimum dose sensitivity (to see the dose above 3 standard deviations of noise) using the impulse response convolved signals were low, resulting in poor dose sensitivities. The sensitivities for 2 Gy radiotherapy fractions and 10 Gy radioimmunotherapy fractions were two orders of magnitude and one order of magnitude higher than the relevant doses, respectively, making thermoacoustic imaging with these transducers impractical for these tasks. Figure 31 shows that at 0.5% noise the image has distortions serious enough to cause enough statistical error to limit the image's usefulness for the aforementioned tasks. However, with the ability to see dose for noise levels below 5.67% (noise level for minimum detector sensitivity), the image for 0.5% noise should clearly be able to be seen (noting that the images in Figure 31 should be interpreted according to noise level and not absolute dose since Eq. 24 and Eq. 25 were used to convert the simulated dose to the corresponding dose levels for transducers with 63 mPa noise). Along these lines, the ability to see the dose ceases around the 5% and 6% noise images in Figure 31, consistent with the calculated noise level of 5.67% for minimum dose sensitivity; although the ability to see dose 3 standard deviations above noise was chosen for this metric to achieve 99.7% confidence, the noise level at which the dose can be seen above the noise level and cannot be seen below the noise level may be subjective.

Figure 32 shows how the images reconstructed with the theoretical signals were much less susceptible to noise-induced distortions than the impulse response images in Figure 31 (note the different noise levels). The dose sensitivities using the theoretical signals were significantly better, which were respectively calculated to be 5.7 Gy, 1.8 Gy, and 0.1 Gy for the three endpoints, compared to 216 Gy, 82 Gy, and 4.9 Gy. While 5.7 Gy is too high for 2 Gy fractions for radiation therapy, 1.8 Gy sensitivity is feasible for achieving 5% statistical error in 10 Gy fractions for radioimmunotherapy. While the LPA proton beam modeled in this thesis only has a Bragg of 0.25 Gy for 10^7 protons/pulse, this represents a lower bound of the possible number of protons/pulse achieved, with the potential to obtain several orders of magnitude greater number of protons/pulse

that could easily 1.8 Gy Bragg peak dose (see Section 2.1). Additionally, the Bragg peak dose of 0.25 Gy could be imaged with a minimum detector sensitivity of 0.1 Gy. Theoretically, the thermoacoustic detector should have great enough sensitivity for these two endpoints, however, accounting for the impulse response shows that the detector does not nearly have enough sensitivity for these endpoints (except for minimum dose sensitivity at 4.9 Gy). The disparity between the theoretical sensitivity and impulse response sensitivity shows how crucial it is for the thermoacoustic signal frequencies to overlap with the transducer center frequency. The theoretical sensitivity was calculated to show the potential for what the impulse response sensitivity could be if transducers with perfect frequency overlap were used instead of the 5 MHz transducers.

7.5 Conclusion

The dose sensitivity to achieve 2% statistical error for 2 Gy radiation therapy fractions was determined to be 216 Gy and 5.7 Gy using the impulse response convolved and theoretical signals, respectively; the sensitivity to achieve 5% statistical error for 10 Gy radioimmunotherapy fractions was determined to be 82 Gy and 1.8 Gy; and the minimum detectable dose sensitivity was determined to be 4.9 Gy and 0.1 Gy. The detector is incapable of being used for 2%/2 Gy fractions since the theoretical sensitivity (i.e., what would be detected with a delta function transducer impulse response that allows for perfect detection of the signals) of 5.7 Gy is greater than 2 Gy. However, the detector has the potential to be used for radioimmunotherapy and general detection of LPA proton doses considering the currently achievable number of protons/pulse. The large differences between the theoretical and impulse response convolved sensitivities highlights both the limitations of the current 5 MHz transducers but also the large potential for improved sensitivity when transducers with bandwidths that better overlap the thermoacoustic signal frequency spectra are implemented.

CHAPTER 8. GENERAL DISCUSSION

Proton beam therapy has shown great promise in cancer treatment and is becoming a more available treatment option. Despite an expanding number of proton facilities, its widespread availability is still limited due to the expensive costs and massive sizes of the cyclotrons/synchrotrons necessary to operate a proton center. LPA proton beams have the potential to expand access to proton therapy for average clinics due to smaller costs and size. However, LPA beam quality is not nearly up to clinical standards and is not likely to see the clinic any time soon, although research continues to figure out how to achieve higher quality beams and to better control them.[4] Even though LPA proton beams may never be able to be achieved with the same monoenergetic quality as cyclotron/synchrotron accelerated beams, advancements in LPA quality may eventually be high enough for clinical use and treatment planning may require different approaches than currently practiced.[23] It would therefore be sagacious to investigate LPA proton beams with their current beam quality for therapeutic purposes.

In addition to accessibility issues, there is significant uncertainty of the proton range in heterogeneous tissues which can be very significant when an OAR is beyond the distal edge of the dose. While extensive QA can be done to ensure accurate beam delivery, *in vivo* dosimetry could reduce the spatial uncertainty; however, there is currently no way to clinically image *in vivo* dose. Measuring annihilation photons from positron emitting radioisotopes and prompt gammas due to proton nuclear interactions has been proposed and has been demonstrated to be feasible.[15–19] However, these modalities are limited in their spatial resolution and sensitivity and are an indirect way of inferring absorbed dose. Thermoacoustic imaging, on the other hand, has the potential for greater resolution and sensitivity while being a direct measurement of the absorbed dose due to collisional stopping power. A previous study in our lab demonstrated the feasibility of thermoacoustic imaging for proton beams modeled based on the proton therapy system at the Indiana University Health Proton Therapy Center (IUHPTC) and imaged with a water-filled cylindrical hydrophone array.[20] For a pencil proton beam with a 20 cm range and 1 μs pulse width, a pressure sensitivity of 38 mPa was needed to measure the range with 1 mm uncertainty with hydrophones for a 1 cGy Bragg peak dose, with a root mean squared dose variation in the Bragg

peak region of 2% between the Monte Carlo (ground truth) dose and reconstructed dose image. For an existing hydrophone with 0.4 MHz bandwidth, a dose sensitivity of 1.6 cGy can be realized.

As an early step towards the end goal of eventual clinical translation to address the issues of proton therapy accessibility and the need for *in vivo* dosimetric imaging, the purpose of this thesis has been to demonstrate the feasibility of integrating LPA proton beams and thermoacoustic imaging into a novel image-guided small animal therapy platform. In this thesis, an LPA proton beam was modeled with characteristics based on literature. Chief among these characteristics is a wide energy spread, which results in lower frequency thermoacoustic waves, with signal frequency being a crucial factor in signal detection. Thermoacoustic waves were simulated from the MC generated LPA proton dose and measured using detectors modeled with in-house detector geometry. Having acquired these signals, a 3D filtered backprojection algorithm was used to reconstruct a volumetric image of the dose. Two significant factors in thermoacoustic imaging are the detector geometry and sensitivity to dose. These two factors were investigated in the three specific aims of this thesis: in Specific Aim 1, the dependence of image accuracy on transducer array angular coverage was investigated; in Specific Aim 2, an iterative reconstruction algorithm was implemented to improve signal sampling for greater image accuracy; and in Specific Aim 3, the detector sensitivity to dose was determined. Based on the results from these specific aims, I believe that the feasibility of integrating LPA proton beams with thermoacoustic imaging for a small animal platform has been demonstrated, although it is necessary that transducers or hydrophones with a center frequency corresponding to the signal frequencies be implemented.

8.1 Specific Aim 1

In Specific Aim 1, the effect of different transducer angular coverages on image accuracy were explored. As a starting point, transducers in the 4π detector KMS256 were incrementally turned off, reducing the total angular coverage, to get an idea of what coverage levels are sufficient. Increasing deviation from the MC dose from 4π to 2π coverage suggested that angular coverage greater than 2π may be needed for sufficiently accurate image reconstruction. Given this, the water levels in the 2π detector KMS128 and sub-2π detector NEXUS128 were shifted inwards towards the detector to effectively get greater angular sampling of projection space. Shifting the water level resulted in image accuracy improvement for both KMS128 and NEXUS128. Notably, a “spike”

artifact at the level of the water edge for NEXUS128 was eliminated by shifting the water level far enough into the detector, having significance for iterative reconstruction in Specific Aim 2. However, unequal weighting of projections by moving the dose off-isocenter resulted in image blurring, although the effects of greater effective sampling may outweigh the effects of blurring. Specific Aim 1 demonstrates that the image accuracy for detectors with insufficient angular coverage may be improved by choice in water level.

8.2 Specific Aim 2

In Specific Aim 2, an iterative reconstruction algorithm was implemented to improve image accuracy through increased projection sampling when angular coverage alone is insufficient for producing accurate images. Iterative reconstruction for the 2π detector NEXUS248 was able to transform a "decent" initial image into a near perfect image of the MC dose; over five iterations, the image converged both in spatial distribution and magnitude to the MC dose. Iterative reconstruction for the sub-2π detector NEXUS128, with the water level shifted inwards by 40 mm to eliminate the "spike" artifact, was able to transform a poor initial image into a "decent" image; over five iterations, the image demonstrated some level of convergence, although complete convergence to the MC dose in spatial distribution and magnitude was not achieved. As occurred in Specific Aim 1, moving the dose off-isocenter resulted in blurring, and the iterative reconstruction algorithm was not able to eliminate it. This is because the algorithm compares the simulated signals to the measured "ground truth" signals, which contain information for the off-isocenter blurring. However, not shifting the water level off-isocenter results in the persistence of the "spike" artifact throughout the iterations as information for this would also be contained in the measured signals. Thus, while the iterative reconstruction algorithm can improve image accuracy, it cannot compensate for insufficient baseline angular coverage. Specific Aim 2 demonstrates that the implementation of an iterative reconstruction algorithm for detectors with angular coverage insufficient for accurate image reconstruction alone may be used to reconstruct high level accuracy images, although a baseline angular coverage is still necessary.

8.3 Specific Aim 3

In Specific Aim 3, the sensitivity of the detectors was determined using transducers with 63 mPa noise at the 5 MHz center frequency. The sensitivities for the therapeutic endpoints of 2% statistical uncertainty for a 2 Gy fraction in radiation therapy, 5% statistical uncertainty for a 10 Gy fraction for radioimmunotherapy, and 78.5% statistical uncertainty for minimum dose sensitivity were theoretically determined to respectively be 5.7 Gy, 1.8 Gy, and 0.1 Gy; however, the inclusion of the transducer impulse response resulted in respective sensitivities of 216 Gy, 82 Gy, and 4.9 Gy as a result of poor correspondence of the transducer center frequency and signal frequencies. This demonstrates how crucial it is for the transducer center frequency to overlap with the signal frequencies; while the signal frequencies cannot be changed without changing the dosimetry, transducers with a lower center frequency could be used to get better sensitivity for the lower frequencies of LPA proton beams. Ideally, the thermoacoustic detector should have a wide bandwidth to cover all relevant frequencies. A wider bandwidth transducer would allow for sensitivity to a wider spectrum of frequencies but the sensitivity at the center frequency would be decreased; there is a tradeoff between bandwidth and center frequency sensitivity. Alternatively, a detector could use a variety of transducers with different center frequencies and hydrophones (which have a low center frequency that overlaps the LPA frequency spectrum) to have high sensitivity over a broad frequency spectrum; a prototype detector in our lab has been built to investigate this. A challenge that would need to be addressed is how to reconstruct an image using the signals measured with heterogeneous frequency sensitivity.

Assuming that the bandwidth of the transducer array can be improved through the implementation of transducers and/or hydrophones better matching the signal frequencies, the theoretically determined sensitivities should be able to be achieved. This work then demonstrates that thermoacoustic imaging can potentially be used for 10 Gy radioimmunotherapy fractions and be able to image the dose in general (minimum detectable sensitivity) using LPA proton beams. The 10^7 protons/pulse modeled results in a Bragg peak dose of 0.25 Gy, which is higher than the minimum detectable dose sensitivity of 0.1 Gy. As discussed in Section 2.1, 10^7 protons/pulse represents a lower bound of the number of protons/pulse achievable with LPA, with higher orders of magnitude number of protons/pulse having the ability to achieve the 1.8 Gy sensitivity for radioimmunotherapy. However, even though LPA proton beams could achieve doses higher than

the 5.7 Gy sensitivity for 2% statistical error for 2 Gy radiotherapy fractions, 5.7 Gy is higher than the planned 2 Gy fraction and so is implausible given the sensitivity.

The sensitivities calculated in this thesis were one to two orders of magnitude dose higher, depending on the endpoint, than the 1.6 cGy achieved by Alsanea et al., which could be sufficient for achieving the statistical errors for all three therapeutic endpoints investigated in this thesis. Direct comparison of the sensitivities is difficult because several factors were different: the use of a monoenergetic 20 cm range proton beam; a 1 μs pulse width; a different endpoint of 1 mm range uncertainty; different detector system (note that the hydrophone bandwidth had good overlap with the signal frequencies); and potential differences in the conversion from pressure to dose. Of these factors, it is likely that the beam energy played a significant role, affecting the relative ratio of the Bragg peak to entrance doses and the generated thermoacoustic waves. These differences could potentially affect the pressure to dose calibration even if the methodology is consistent. Future work will need to be performed while controlling for the different factors to determine the exact reasons for the disparity.

8.4 Limitations

There are several assumptions made in this thesis. Notably, the LPA proton beam was not an actual LPA simulation but was modeled to have characteristics based on literature. While many key characteristics are given in articles, no article tries to describe every parameter of the beam they achieved but rather answer a specific question about LPA, and so LPA characteristics could not be modeled based on a single article. The LPA beam that was modeled therefore represents characteristics from several different beams in literature. While some parameters are easier to model, such as the total number of protons/pulse, other parameters are more difficult to model. In particular, modeling the energy spread poses a challenge since it may be irregular. A continuous energy distribution with a gradual falloff and distinct cutoff energy, while presented in several articles,[7–9] was not modeled as such a beam would not be feasible, without some kind of energy selector, for use in radiation therapy. Because several articles presented energy spectra with peaks and reported FWHMs,[5,6,11,14] a Gaussian profile beam was selected to model this kind of spectrum, although the actual spectrums may not be perfectly Gaussian. This choice in modeling a Gaussian energy spread, although it represents a simplified energy distribution, is not without merit. For use

in thermoacoustic imaging, the frequency distribution of the dose is crucial to detection due to transducer bandwidths. Whatever the actual energy distribution of an LPA beam may be, the fact that the energy spectrum is wide means that the dose distribution will have less a steep distal edge falloff and lateral penumbra which will result in lower frequency signals. The major difference in this thesis from the previous study in our lab by Alsanea et al.,[20] other than detector geometry, is that they modeled a monoenergetic pencil proton beam which has a sharp Bragg peak and penumbra that results in higher frequency signals than an LPA beam would have. While they demonstrated the feasibility of thermoacoustic imaging for monoenergetic proton beams, the proton beam modeled in this thesis determines the feasibility of thermoacoustically imaging a proton beam with a wide energy spread, of which an LPA proton beam falls into this category. In future studies, an actual LPA proton beam could be simulated, such as with particle in cell (PIC) simulations.

Several assumptions were made regarding thermoacoustic imaging as well. The simulation of the thermoacoustic pressure waves assumes a homogeneous speed of sound. This may be an accurate assumption in uniform phantoms such as water, however, the speed of sound may be inhomogeneous in different tissues, which may result in, for example, signals originating at the same distance from a transducer arriving at different times, decreasing the resolution. Methods have been developed to correct for this such as by applying a homogeneous medium calibration correction to the signal arrival time[28] or using speed of sound distribution maps determined by x-ray CT with iterative reconstruction.[29] Additionally, the filtered backprojection algorithm assumes transducers that are spatially points, not accounting for the finite size of the transducers. A signal from a point source will reach different areas of the transducer surface at different times due to slight differences in travel distance, resulting in potentially significant blurring in the image.[30] Techniques have been developed to correct for the finite transducer size by deconvolution of the spatial impulse response[31] or by model-based iterative reconstruction algorithms.[32,33] Acoustic attenuation was also assumed to be negligible, which may be valid for temperature controlled water though may be more pronounced in heterogeneous tissues. Acoustic attenuation results in a lower measured signal with higher frequencies being differentially attenuated (which also reduces spatial resolution); this may be less significant for LPA proton beams than monoenergetic proton beams since the lower frequency signals of the LPA beams are relatively less affected by acoustic

attenuation. Acoustic attenuation and dispersion (different speed of sounds for different frequencies) have been modeled and corrected for with time-reversal reconstruction.[34]

8.5 Future Work

Because differences in the stopping powers and physical models utilized in MC code could result in differences in the dose, it is important to compare the MC dose results from FLUKA to other MC programs, such as the widely used program GEANT4. GEANT4 is an object-oriented MC toolkit that allows for the easy implementation of different physics models.[35] One study found that the differences in depth dose profiles between FLUKA and GEANT4 for monoenergetic proton beams were small, although there were minor discrepancies when small Gaussian energy spreads were introduced.[36] Although these discrepancies were < 0.5%, there is potential that the wider energy spreads of LPA proton beams could result in greater discrepancies. Additionally, the production of secondary particles, such as neutrons and prompt gammas, can be significantly different between the two programs.[37] Future work will compare the dose from LPA proton beams from FLUKA and GEANT4.

In addition to proton therapy, carbon ion therapy has the potential to augment the dosimetric and radiobiological properties produced by protons.[38] Carbon ions, instead of having +1e charge like protons, have up to +6e charge; Eq. 19 shows that the stopping power is proportional to the square of the effective charge of the ion, so the higher charge of carbon ions results in a much higher stopping power that results in higher LET and RBEs. Additionally, because the mass is heavier than protons, carbon ions have less angular deflection when scattered which results in a sharper Bragg peak and lateral penumbra. However, sharing similar advantages to proton therapy, carbon ion therapy also shares the same disadvantages such as the requirement of massive and expensive cyclotrons/synchrotrons for acceleration to therapeutic energies; the widespread use of carbon ion therapy is even more limited than for proton therapy. Likewise, LPA has the potential to make carbon ion therapy more accessible. If a proton-poor, carbon-rich target is used, more carbon ions will be able to be accelerated before the space charge between the “hot” electrons and ions is terminated.[8] One study was able to experimentally achieve carbon ions with 48 MeV/u, with protons contaminating the beam having 58 MeV;[39] this study reported that acceleration schemes using the RPA mechanism may reduce proton contamination compared to

the TNSA mechanism. However, the 48 MeV/u has a range < 1 cm,[40] so higher energies are still needed for therapeutic applications. Another study was able to simulate 817 MeV/u carbon ions,[14] although the laser intensity was several orders of magnitude greater than used experimentally. Future work will seek to model LPA carbon ion beams and investigate its detectability with thermoacoustic imaging.

In Specific Aims 1 and 2, it was mentioned several times that the images were blurred when they were moved off-isocenter. To help conceptualize, refer to Figure 14. The spherical detector was designed so that the projections are equally weighted at isocenter. When the water level was shifted inwards off-isocenter, the dose was moved to a position in the detector where the projections are more laterally weighted and less longitudinally weighted due to the angles at which the projections pass through the dose. Additionally for large enough water level shifts, if two transducers have a symmetric azimuthal angle relative to a transverse plane centered on the dose, when the detector is polarly rotated so that the transducers have a polar angle of 180° between them (in projection space), the projection will be the same and have twice the weighting. The further the water level is shifted inwards, the more pairs of transducers will have symmetric azimuthal angles. This leads to unequal projection weighting and subsequently off-isocenter blurring. Adjusting the weights of each transducer depending on its azimuthal angle, polar angle, and water level may be able to correct for this blurring. Alternatively, the blurring may be able to be corrected for based on the detector point spread function. Future studies will seek to correct for the off-isocenter blurring.

CHAPTER 9. CONCLUSION

The feasibility of integrating LPA proton beams and thermoacoustic imaging into an image-guided small animal therapy platform has been demonstrated. An MC method was used to simulate a proton beam with LPA characteristics based on literature, thermoacoustic pressure waves were simulated from the MC dose, and 3D filtered backprojection was used to reconstruct volumetric dose images. Specific Aim 1 investigated the dependence of image accuracy on transducer array angular coverage, including the effect of shifting the water level off-isocenter, and Specific Aim 2 implemented an iterative reconstruction algorithm to improve image accuracy when transducer array angular coverage is insufficient. Together, Specific Aims 1 and 2 demonstrate the feasibility of accurately reconstructing the spatial distribution and magnitude of LPA proton beam dose using spherical geometry detectors with limited, potentially sub-2π, angular coverage. Specific Aim 3 investigated the detector dose sensitivity, with LPA beams having the potential to achieve doses higher than the sensitivities for 10 Gy radioimmunotherapy fractions and minimum detectable sensitivity. The sensitivities when accounting for the transducer impulse response were unacceptably poor, demonstrating the need to use transducers and/or hydrophones with center frequencies that overlap the thermoacoustic signal frequency spectrum. Future studies will seek to use transducers and hydrophones with bandwidths that better match the thermoacoustic signals, implement more realistic LPA models, and correct for off-isocenter blurring.

REFERENCES

1. Choi, D. K., Helenowski, I. & Hijiya, N. Secondary malignancies in pediatric cancer survivors: Perspectives and review of the literature. *Int. J. Cancer* **135**, 1764–1773 (2014).

2. Miles, D. *et al.* Differential effects of high versus low linear energy transfer (LET) radiation on type-I interferon (IFNβ) and TREX1 responses. (2021).

3. Particle therapy facilities in clinical operation. *Particle Therapy Co-Operative Group* (2022).

4. Karsch, L. *et al.* Towards ion beam therapy based on laser plasma accelerators. *Acta Oncol. (Madr).* **56**, 1359–1366 (2017).

5. Schwoerer, H. *et al.* Laser-plasma acceleration of quasi-monoenergetic protons from microstructured targets. *Nature* **439**, 445–448 (2006).

6. Meinhold, T. A. & Kumar, N. Radiation pressure acceleration of protons from structured thin-foil targets. *J. Plasma Phys.* **87**, (2021).

7. Wagner, F. *et al.* Maximum Proton Energy above 85 MeV from the Relativistic Interaction of Laser Pulses with Micrometer Thick CH2 Targets. *Phys. Rev. Lett.* **116**, 1–5 (2016).

8. Macchi, A., Borghesi, M. & Passoni, M. Ion acceleration by superintense laser-plasma interaction. *Rev. Mod. Phys.* **85**, 751–793 (2013).

9. Higginson, A. *et al.* Near-100 MeV protons via a laser-driven transparency-enhanced hybrid acceleration scheme. *Nat. Commun.* **9**, (2018).

10. Cowan, T. E. *et al.* Ultralow emittance, multi-MeV proton beams from a laser virtual-cathode plasma accelerator. *Phys. Rev. Lett.* **92**, 1–4 (2004).

11. Sharma, A. & Kamperidis, C. High energy proton micro-bunches from a laser plasma accelerator. *Sci. Rep.* **9**, 1–10 (2019).

12. Robson, L. *et al.* Scaling of proton acceleration driven by petawatt-laser-plasma interactions. *Nat. Phys.* **3**, 58–62 (2007).

13. Kawata, S. *et al.* Laser ion acceleration toward future ion beam cancer therapy-Numerical simulation study. *Laser Ther.* **22**, 103–114 (2013).

14. Mirzanejhad, S., Sohbatzadeh, F., Joulaei, A., Babaei, J. & Shahabei, K. Optimization of laser acceleration of protons from mixed structure nanotarget. *Laser Part. Beams* **33**, 339–346 (2015).

15. Knopf, A. C. & Lomax, A. In vivo proton range verification: A review. *Phys. Med. Biol.* **58**, 131–160 (2013).

16. Min, C. H., Lee, H. R., Kim, C. H. & Lee, S. B. Development of array-type prompt gamma measurement system for in vivo range verification in proton therapy. *Med. Phys.* **39**, 2100–2107 (2012).

17. Min, C. H., Kim, C. H., Youn, M. Y. & Kim, J. W. Prompt gamma measurements for locating the dose falloff region in the proton therapy. *Appl. Phys. Lett.* **89**, 2–5 (2006).

18. Moteabbed, M., España, S. & Paganetti, H. Monte Carlo patient study on the comparison of prompt gamma and PET imaging for range verification in proton therapy. *Phys. Med. Biol.* **56**, 1063–1082 (2011).

19. Vynckier, S. *et al.* Is it possible to verify directly a proton-treatment plan using positron emission tomography? *Radiother. Oncol.* **26**, 275–277 (1993).

20. Alsanea, F., Moskvin, V. & Stantz, K. M. Feasibility of RACT for 3D dose measurement and range verification in a water phantom. *Med. Phys.* **42**, 937–946 (2015).

21. Lyamshev, L. M. Radiation Acoustics. *Sov. Phys. Uspekhi* **35**, 276–302 (1992).

22. Kruger, R. A., Liu, P., Fang, Y. 'Richard' & Appledorn, C. R. Photoacoustic ultrasound (PAUS)--Reconstruction tomography. (1995).

23. Schell, S. & Wilkens, J. J. Advanced treatment planning methods for efficient radiation therapy with laser accelerated proton and ion beams. *Med. Phys.* **37**, 5330–5340 (2010).

24. Andreo, P., Burns, D. T., Nahum, A. E., Seuntjens, J. & Attix, F. H. *Fundamentals of Ionizing Radiation Dosimetry*. (Wiley-VCH, 2017).

25. Gibbons, J. P. *Khan's The Physics of Radiation Therapy*. (Wolters Kluwer Health, 2020).

26. Battistoni, G. *et al.* The FLUKA code: An accurate simulation tool for particle therapy. *Front. Oncol.* **6**, (2016).

27. National Institute of Standards and Technology. PSTAR: Stopping Power and Range Tables for Protons.

28. Manohar, S., Willemink, R. G. H., Van Der Heijden, F., Slump, C. H. & Van Leeuwen, T. G. Concomitant speed-of-sound tomography in photoacoustic imaging. *Appl. Phys. Lett.* **91**, 1–4 (2007).

29. Huang, C., Wang, K., Nie, L., Wang, L. V. & Anastasio, M. A. Full-wave iterative image reconstruction in photoacoustic tomography with acoustically inhomogeneous media. *IEEE Trans. Med. Imaging* **32**, 1097–1110 (2013).

30. Kiser, Jr., W. L. & Kruger, R. A. Thermoacoustic computed tomography: limits to spatial resolution. in *Medical Imaging 1999: Physics of Medical Imaging* **3659**, 895–905 (1999).

31. Li, M.-L. & Cheng, C.-C. Reconstruction of photoacoustic tomography with finite-aperture detectors: deconvolution of the spatial impulse response. *Photons Plus Ultrasound Imaging Sens. 2010* **7564**, 75642S (2010).

32. Wang, K. *et al.* An imaging model incorporating ultrasonic transducer properties for three-dimensional optoacoustic tomography. *IEEE Trans. Med. Imaging* **30**, 203–214 (2011).

33. Rosenthal, A., Ntziachristos, V. & Razansky, D. Model-based optoacoustic inversion with arbitrary-shape detectors. *Med. Phys.* **38**, 4285–4295 (2011).

34. Treeby, B. E., Zhang, E. Z. & Cox, B. T. Photoacoustic tomography in absorbing acoustic media using time reversal. *Inverse Probl.* **26**, (2010).

35. Agostinelli, S. *et al.* GEANT4 - A simulation toolkit. *Nucl. Instruments Methods Phys. Res. Sect. A Accel. Spectrometers, Detect. Assoc. Equip.* **506**, 250–303 (2003).

36. Yang, Z. Y. *et al.* Inter-comparison of Dose Distributions Calculated by FLUKA, GEANT4, MCNP, and PHITS for Proton Therapy. *EPJ Web Conf.* **153**, 1–8 (2017).

37. Robert, C. *et al.* Distributions of secondary particles in proton and carbon-ion therapy: A comparison between GATE/Geant4 and FLUKA Monte Carlo codes. *Phys. Med. Biol.* **58**, 2879–2899 (2013).

38. Kim, J., Park, J. M. & Wu, H.-G. Carbon Ion Therapy: A Review of an Advanced Technology. *Prog. Med. Phys.* **31**, 71–80 (2020).

39. Ma, W. J. *et al.* Laser Acceleration of Highly Energetic Carbon Ions Using a Double-Layer Target Composed of Slightly Underdense Plasma and Ultrathin Foil. *Phys. Rev. Lett.* **122**, 1–6 (2019).

40. Hiraoka, T. & Bischel, H. Stopping powers and ranges for heavy ions. *Japanese J. Med. Phys.* **15**, 91–100 (1995).